LBNL-39803
UC-1501

ERNEST ORLANDO LAWRENCE
BERKELEY NATIONAL LABORATORY

Exploratory Fuel-Cell Research: I. Direct-Hydrocarbon Polymer-Electrolyte Fuel Cell II. Mathematical Modeling of Fuel-Cell Cathodes

Michael L. Perry,* Frank R. McLarnon,
John S. Newman, and Elton J. Cairns
Energy and Environment Division

December 1996
*M.S. Thesis

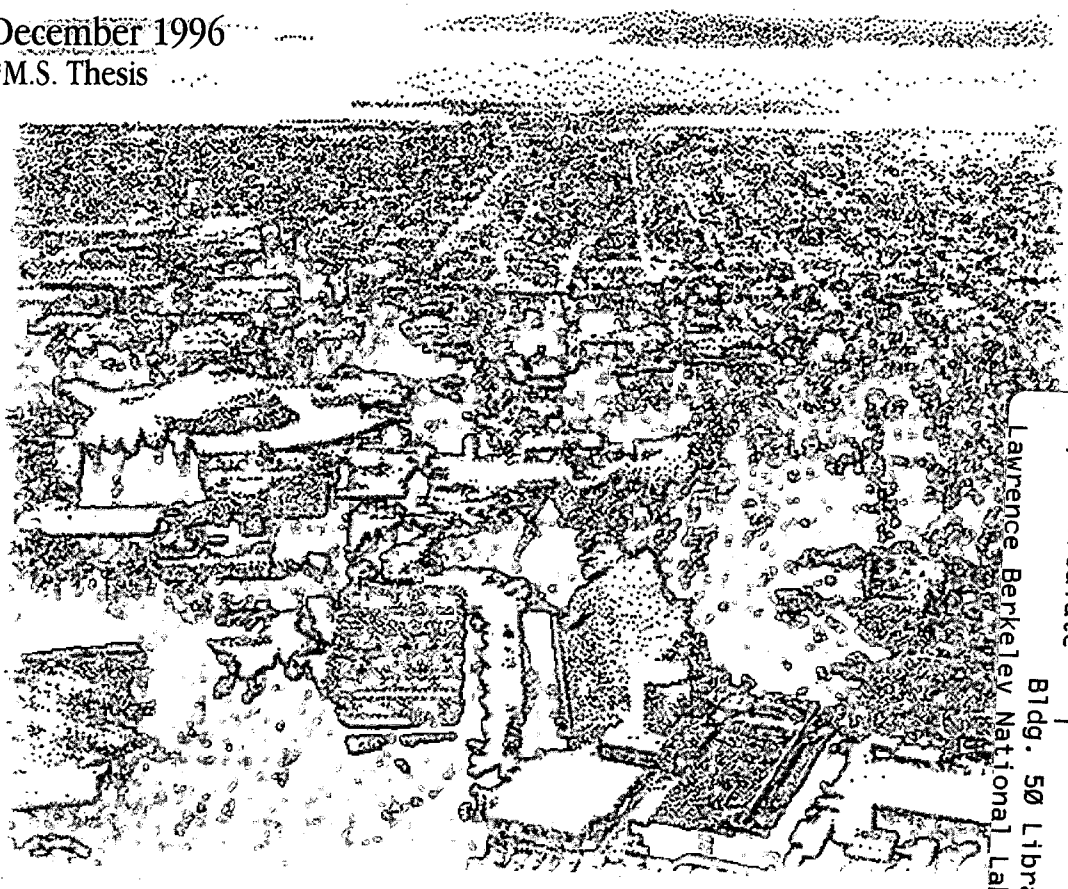

DISCLAIMER

LBNL-39803
UC-1501

Exploratory Fuel-Cell Research:

I. Direct-Hydrocarbon Polymer-Electrolyte Fuel Cell

II. Mathematical Modeling of Fuel-Cell Cathodes

by

Michael L. Perry,* Frank R. McLarnon

John S. Newman and Elton J. Cairns

*M.S. Thesis

Department of Chemical Engineering
University of California

and

Energy & Environment Division
Lawrence Berkeley National Laboratory
Berkeley, California 94720

December 1996

This work was supported by the Assistant Secretary for Energy Efficiency and Renewable Energy, Office of Transportation Technologies, Office of Advanced Automotive Technologies of the U.S. Department of Energy under Contract No. DE-AC03-76SF00098.

Dedicated to the memory of

Professor Charles W. Tobias

(1920 — 1996)

A modern-day Renaissance Man,

whose passion for life will continue to inspire me

to be much more than just a good engineer.

Table Of Contents

List of Figures

List of Tables

Acknowledgments

What a long, strange trip it's been. — The Grateful Dead

I realize that this part of a M.S. Thesis should probably be rather short, however since my work here has now encompassed a period of over a decade (most of which I fortunately did not spend in school) I feel that the length is somewhat justified.

First, and foremost, is Professor Cairns who played an instrumental role in my return to this department after my extended "sabbatical" in the Navy. I thank him for believing in my abilities. He also provided me with challenging research topics that made me to think beyond what was written in the literature. I also wish to thank both him and Dr. Frank McLarnon for their patient advice and for sharing their wealth of knowledge on fuel cells and batteries with me.

Professor Newman not only was my principle advisor for the modeling portion of this work, but also was undoubtedly the single greatest contributor to my education as an electrochemical engineer. Many of the myriad of important concepts that are packed into his concise textbook were finally instilled in me through his courses, Wednesday night seminars, group meetings, and summer reading sessions. I wish to thank him for his open-door policy, which was a great benefit to me.

There are many past and present members of the LBNL Electrochemistry Research Group, as well as Prof. Newman's group, that also contributed to my education and made my stay here more enjoyable. In particular, I would like to thank Dr. Kathy Striebel for

some very helpful discussions and her encouragement. Special thanks to Bava Pillay, Kathy Ta, Gerd Matzen, Rob Darling, and Jeremy Meyers for interesting conversations and for helping me brush off some programming cobwebs. David Beltran was also instrumental in helping me with this work, both in the lab and on a PC.

I owe a large debt of gratitude to my parents, the true depth of which I am just beginning to fathom, who instilled in me the belief that I could become anything I wanted, and who have supported me on the paths I have chosen. They also have the rather dubious honor of providing me with one of my major motivations for this work — a childhood in the Los Angeles basin prior to the introduction of the catalytic converter. (I should also thank the Navy for inspiring this research, my "all-expenses-paid cruise" to the Middle East exposed me to the true price we pay for crude oil.)

Finally, and most importantly, I wish to thank my wife for her unwavering support. Her words of encouragement kept me on track, and she kept this track full of fun and adventure. She also provided me with the greatest and most wonderful inspiration of all, a beautiful baby daughter. This work is ultimately for my daughter's generation. Perhaps her first car will be an electric vehicle; at least I won't have to teach her how to change the oil.

This work was supported by the Assistant Secretary for Energy Efficiency and Renewable Energy, Office of Transportation Technologies, Office of Advanced Automotive Technologies of the U.S. Department of Energy under Contract No. DE-AC03-76SF00098.

Chapter 1. Introduction

"When the well's dry, we know the worth of water." — Benjamin Franklin

1.1 Fuel Cells and the Need for Efficient Energy-Conversion Devices

A strong need exists today for more efficient energy-conversion systems. Our reliance on limited fuel resources, such as petroleum, for the majority of our energy needs makes it imperative that we utilize these resources as efficiently as possible. Higher-efficiency energy conversion also means less pollution, since less fuel is consumed and less exhaust created for the same energy output. Additionally, for many industrialized nations, such as the United States which must rely on petroleum imports, it is also imperative from a national-security standpoint to reduce the consumption of these precious resources. A substantial reduction of U. S. oil imports would result in a significant reduction of our trade deficit, as well as costly military spending to protect overseas petroleum resources. Therefore, energy-conversion devices which may utilize alternative fuels are also in strong demand.

Fuel cells are the only energy-conversion devices which convert chemical energy directly into electrical energy, without the intermediary of heat. Therefore, fuel cells offer high theoretical efficiencies compared to devices that burn the fuel, like gas turbines or internal-combustion engines. Fuel cells are also capable of operating with a wide variety of fuels, either directly or indirectly.

In principle, the operation of a fuel cell is very simple. It is an electrochemical device which can supply energy continuously as long as it is supplied with fuel and oxidant. Fig. 1-1 is a schematic diagram of a fuel cell with an acid electrolyte.

Negative Electrode (Anode):

$H_2 \longrightarrow 2\,H^+ + 2\,e^-$

1. Hydrogen gas enters the fuel cell at the anode.
2. The hydrogen molecules adsorb onto the anode catalyst, and are converted into protons and electrons.
3. The protons migrate through the acid electrolyte towards the cathode.
4. The electrons, flowing down a potential gradient, perform useful work via the external circuit (*i.e.*, they power an electric motor for an electric vehicle).

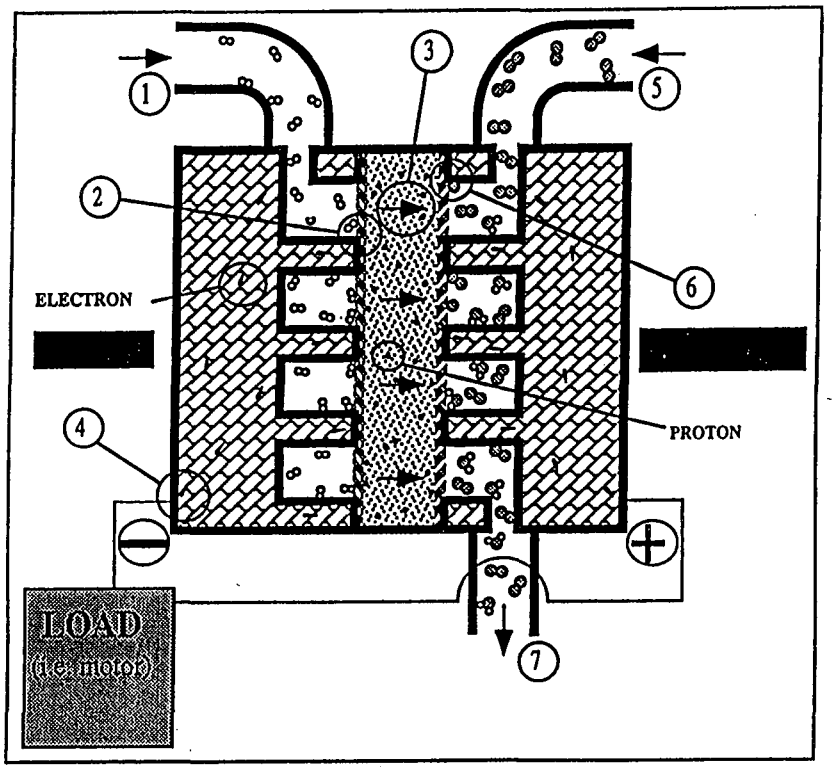

Positive Electrode (Cathode):

$2\,H^+ + \tfrac{1}{2}\,O_2 + 2\,e^- \longrightarrow H_2O$

5. Air (containing oxygen) enters the fuel cell at the cathode.
6. The oxygen molecules adsorb onto the cathode catalyst. The oxygen reacts with the protons and electrons to form water.
7. The product water and excess gas exit the fuel cell.

Overall Reaction:

$H_2 + \tfrac{1}{2}\,O_2 \longrightarrow H_2O$

Figure 1-1. Schematic diagram illustrating the basic principles of an acid-electolyte fuel cell operating on hydrogen and air.
(Adapted from: M. DeLuchi and D. Swan, "The Promise of Fuel-Cell Vehicles," *Access*, 3, 1993.)

Fuel cells have been the subject of many excellent books [1,2], monographs [3], and review articles [4,5], and therefore their basic operating principles will not be elaborated on here.

1.2 Fuel Cells for Transportation Applications

. In the U. S., transportation consumes over 60% of the petroleum used, and highway vehicles account for over 75% of this consumption [6]. Petroleum-fueled vehicles are also responsible for two-thirds of the carbon-monoxide emissions in the U. S., as well as significant fractions of the NO_x, lead, CO_2, volatile organic compounds, and particulates [7]. Since fuel cells operate more efficiently than internal-combustion engines, and produce less potentially harmful products, the introduction of fuel-cell-powered vehicles could have a major impact on both petroleum consumption and pollution concerns.

For transportation applications, fuel cells with low operating temperatures are required, in order to minimize start-up times. However, state-of-the-art low-temperature ($< 200^0$C) fuel cells are close to achieving the specific power and efficiency required for transportation applications only when operating on a hydrogen fuel source. Therefore, either a hydrogen-storage device or a fuel reformer must be carried onboard the vehicle. Currently, hydrogen is a relatively expensive fuel, and it cannot be stored in a compact or lightweight manner. Fuel reformers add complexity, volume, and cost to the system; and there is the additional problem that the CO in the reformate may poison the catalyst. Both of these hydrogen-delivery options result in a power plant that is too heavy, bulky, and costly to compete with the internal-combustion engine. A strong need therefore exists for

a low-temperature fuel cell that can electrochemically oxidize more easily transported fuels, especially liquid fuels since these may be stored in a more compact manner than gases such as hydrogen.

Hydrocarbons are readily available and inexpensive fuels; in addition, propane and larger homologs may be conveniently stored as a liquid. However, it is a widely held view that low-temperature fuel cells cannot directly oxidize hydrocarbons at rates that are of any practical interest [5]. Next to hydrogen, methanol appears to be the most suitable fuel for low-temperature fuel cells, since it can be electrochemically oxidized much more readily than hydrocarbons at low temperatures. Methanol is readily available, can be produced from a variety of sources, and is a liquid at ambient temperature.

The most promising fuel cells for transportation applications appear to be the polymer-electrolyte fuel cell (PEFC) and the alkaline-electrolyte fuel cell (AFC). They are the only low-temperature fuel cells capable of attaining high power densities (> 1 W/cm^2), primarily because they provide the best oxygen reduction reaction (ORR) rates at low temperatures [8]. Both of these systems have been successfully employed in the U. S. space program, operating on pure hydrogen and oxygen. However, developing these systems to operate on fuels other than hydrogen, at practical costs and high power densities, has proven to be a greater challenge. For example, methanol readily permeates the polymer electrolyte of a PEFC and oxidizes at the cathode, which significantly degrades the overall fuel-cell efficiency, in addition to adversely affecting the performance of the cathode. In the case of an AFC, the carbon dioxide that is formed by the oxidation of carbon-containing fuels reacts with the alkaline electrolyte to form carbonates, which precipitate and effectively destroy the AFC.

1.2 Scope and Organization of this Thesis

The purpose of the first part of this research was to explore an alternative fuel-cell technology that could potentially avoid the inherent pitfalls of the two systems just mentioned. For reasons that will be fully explained in the following chapter, we attempted to operate a PEFC directly on hydrocarbon fuels. Since the results of this work were discouraging, it was abandoned at an early stage in order to work on more-promising possibilities. Initially, this redirection involved the continuation of on-going work in our laboratory on the direct-methanol aqueous-carbonate fuel cell (DMACFC) [9]. However, this DMACFC work led to an interesting question regarding the results of the previous modeling work that had been done on the cathode of this type of fuel cell [10, 11]. In particular, it became apparent that these modeling results predicted a different oxygen concentration dependence for the ORR when the cathode is rate limited by the mass transport of ions participating in the ORR. The significance of this result had not been emphasized in previous work, and thus it was felt that further modeling was justified to determine the general applicability of this result to this and other more common fuel-cell systems. This modeling work led to the development of a new diagnostic tool that may be used to analyze fuel-cell data to determine whether the mass transport of oxygen and/or ions is controlling a fuel-cell cathode at moderate to high current densities.

The results of both the experimental direct-hydrocarbon PEFC work and the modeling work are the subject of this thesis.

The next chapter provides more extensive background and motivation for both portions of this work. Chapter 3 describes the experimental procedures and apparatus used to conduct the PEFC experiments, as well as the results of these experiments. Also

included in this chapter are some conclusions and recommendations regarding a direct-hydrocarbon PEFC.

The modeling work is presented in Chapter 4, along with a discussion and a physical explanation of the results of this work. Chapter 5 outlines how the results of the modeling work may be used as a diagnostic tool for analyzing fuel-cell data. The proposed tool is also demonstrated in this final chapter by analyzing cathode data from the literature for two different types of fuel cells.

Chapter 2. Background and Research Objectives

"Whatever nature has in store for mankind, unpleasant as it may be, men must accept, for ignorance is never better than knowledge." — Enrico Fermi

2.1 Polymer-Electrolyte Fuel Cell (PEFC)

Despite the successful application of a PEFC in the U. S. Gemini space program, further development of this type of fuel cell was not actively pursued for many years primarily because of two major problems. One problem was the limited lifetime of the polymers that were employed in these early cells. These early ion-exchange membranes were hydrocarbon-based polymers, such as polystyrene-divinylbenzene-sulfonic acid (cross-linked within an inert flourocarbon film), which were prone to oxidative degradation due to cleavage of the C-H bonds. This factor also restricted the operating temperature of these PEFC's to less than 75° C. The other major problem was the high catalyst loadings required in a PEFC relative to liquid-electrolyte fuel cells. (The Gemini fuel cells used a catalyst loading of 35 mg/cm^2 of Pt black, which was bonded to a gold screen with PTFE; whereas early PEFC's with Nafion® utilized about 4 mg/cm^2 of Pt black in each electrode [12].)

Two relatively recent developments have greatly renewed interest in PEFC's. The first was the development of Nafion® by E. I. du Pont de Nemours. Nafion® is a perflourosulfonic-acid ion-exchange membrane which is electrochemically stable at temperatures up to at least 130° C. It consists of a PTFE-backbone chain with perflourinated-vinyl-polyether side chains that terminate in sulfonate groups which provide

the cation-exchange sites. Nafion® was not specifically developed for use in fuel cells; it was instead produced for the chloroalkali industry. However, many researchers recognized that this robust polymer would be well suited for other applications. Yeo has provided an excellent review of the physical properties of Nafion® which are relevant to its electrochemical applications [13]; and Grot has provided an overview of the many applications for which Nafion® is being considered [14].

Even with the introduction of Nafion®, the problem of high catalyst loadings still remained a large obstacle to the commercial development of a PEFC. The problem was that the interface between the electrolyte membrane and the adjoining electrodes was essentially two-dimensional. Therefore, the only catalyst that was being effectively utilized was the surface layer that was in physical contact with the ion-conducting polymer. In the case of liquid electrolytes, the porous electrodes are ideally partially flooded with electrolyte, thereby providing a more three-dimensional active region and a much higher catalyst utilization. Raistrick at Los Alamos National Laboratory (LANL) recognized this important difference and provided a solution to the problem by using Nafion® ionomer in the liquid form to penetrate the PTFE-bonded catalyst layer of a conventional gas-diffusion electrode [15]. He also demonstrated that this technique could effectively provide equivalent performance with an order-of-magnitude less catalyst (0.35 *vs.* 4 mg Pt/cm^2) than conventional electrodes [16]. This development greatly renewed interest in the PEFC, since catalyst cost was no longer prohibitive for this technology. In fact, with these low catalyst loadings, the polymer and the bipolar plates are now the most expensive components of the PEFC.

As mentioned in the introduction to this thesis, PEFC's are capable of high power densities because the ORR kinetics are relatively fast. In fact, the exchange current densities for oxygen reduction with Nafion® are the highest for any acid electrolyte at low temperatures [17]. It is generally held that alkaline electrolytes provide better oxygen reduction performance than acids because competitive anion adsorption on the electro-catalyst is minimal compared to acids [8, 17]. The superior ORR performance with a perflourosulfonic-acid electrolyte is therefore largely attributed to the lower competitive anion adsorption at the cathode with the polymer electrolyte, since the anions are tied to the polymer chain.

PEFC's have many other advantages over fuel cells with liquid electrolytes. Namely, they are simple to fabricate, corrosion problems are less severe, resistance losses are low with the use of very thin membranes, large pressure differentials can be employed, and they have demonstrated long lifetimes.

2.1.1 Direct-Methanol Polymer-Electrolyte Fuel Cell

The PEFC is an especially attractive system for mobile applications because of its low operating temperature and the advantages stated above [6]. Therefore, it is not surprising that many researchers are attempting to develop a PEFC that will operate with methanol as a fuel. However, there are some serious problems with the direct-methanol PEFC that must be overcome before this technology is viable.

The first major problem is shared by all low-temperature direct-methanol fuel cells (DMFC's), namely the relatively sluggish kinetics of methanol oxidation compared to hydrogen. Methanol anodic-oxidation rates are several orders of magnitude below that of

hydrogen on a Pt catalyst [5]. Some undesirable oxidation products, such as formic acid and formaldehyde, may also be produced instead of carbon dioxide and water, especially in acid electrolytes. Additionally, methanol dissolved in the polymer electrolyte will cross over to the cathode by diffusion and electroosmotic drag, where it reacts with oxygen to produce heat. This cross over not only lowers the overall efficiency of the DMFC, but it also adversely affects the cathode performance [18, 19]. This last problem is especially severe with the perflourosulfonic-acid ion-exchange membranes, since these membranes must be kept hydrated to maintain their ionic conductivity and methanol is completely miscible with water.

2.2 Direct-Hydrocarbon Fuel Cells

The anodic-oxidation rates of hydrocarbons are even lower than that of methanol on a Pt catalyst. However, it was shown in the 1960's that the complete oxidation of alkanes (methane through hexadecane) at moderate current densities (10 to 500 mA/cm^2) and practical overpotentials (< 0.5 V *vs.* RHE) can be achieved in strong-acid electrolytes (HF, H_2SO_4, and $HClO_4$) at temperatures below 200^0C, with high loadings of Pt or Pt-alloy catalysts (2.5 to 50 mg/cm^2) [20]. It was also determined that alkanes yield higher current densities than their corresponding alkenes and alkynes, and the best oxidation rates were obtained with propane. An excellent summary of this work has been provided by Cairns [20].

One of the important conclusions of this early work was that the identity and concentration of the electrolyte has a profound effect on the overall rate of oxidation of alkanes (which are relatively weakly and slowly adsorbed), but only a modest effect on the

rate of oxidation of the alkenes and alkynes (which are strongly and rapidly adsorbed). The significant differences in alkane oxidation rates among different acid electroytes were found to be opposite the tendencies of the acid anions to adsorb on platinum [21]. These results are consistent with the idea that the acid anions competitively adsorb on the platinum surface and thereby hinder the desired reaction, especially with a reactant which is weakly adsorbed.

As mentioned above, it is postulated that one of the primary reasons that a perflourosulfonic-acid (PFSA) electrolyte, such as Nafion®, supports relatively high ORR rates is the fact that the sulfonate anions are tied to the polymer chain and therefore competitive anion adsorption at the cathode is minimized. Therefore, we hypothesized that a PFSA electrolyte might also support high anodic oxidation rates with hydrocarbons, especially the weakly adsorbed alkanes like propane. Additionally, the aforementioned cross-over problem associated with the direct-methanol PEFC would be expected to be relatively insignificant with a direct-hydrocarbon PEFC, since hydrocarbons have a low solubility in water and therefore the electroosmotic drag should be relatively low. These factors, along with the availability and ease of transport of hydrocarbons, motivated this study.

2.2.1 Research Objectives for the Direct-Hydrocarbon PEFC

An experimental program was initiated to investigate the anodic oxidation rates of hydrocarbons with a Nafion® electrolyte. The expectation was that these rates would be higher than those previously obtained with liquid-acid electrolytes, and that this superior performance might be good enough to justify renewed interest in a low-temperature,

direct-hydrocarbon fuel cell. It was felt that because of the simplicity of this system, and the availability of inexpensive hydrocarbon fuels, that the performance gains required for a practical system were modest; and, for the reasons given above, that such gains might be achieved with a state-of-the-art PEFC.

2.3 Porous Gas-Diffusion Electrodes

Porous electrodes are commonly employed in many electrochemical applications because they provide large and intimate interfacial contact of the electrode material with the electrolyte phase. This large area per unit volume can help compensate for the intrinsically slow rates of heterogeneous electrochemical reactions (particularly the ORR or the anodic oxidation of hydrocarbons) and thereby result in acceptable current densities (based on the geometric area of the electrode) and reduce the ohmic potential drop by reducing the distance this current must flow.

In a gas-diffusion electrode (GDE), three species must be transported to or from the electrocatalyst sites in order for the heterogeneous electrochemical reactions to occur on a continuous basis. These species are: 1) the electrons in the solid matrix, 2) the ions in the solution, and 3) the gases dissolved in the solution. Only the catalyst sites which are in contact with the solution (and the ions therein) will be active; which is why the reactant gases must be dissolved to participate in the reaction,* and the products of the reaction will also be produced in the solution phase. Since each of these species must be transported either to or from the catalyst sites, mass transport may control the rate of the

* Although adsorption followed by surface diffusion may also provide for a continuous reaction.

reaction, in addition to kinetics; and therefore reaction rates throughout a GDE tend to be nonuniform, especially at high current densities.

Mass-transport limitations in a porous electrode with a reaction obeying Tafel kinetics can result in a double Tafel slope. In flooded-porous electrodes two distinct limiting cases have been shown to cause a double Tafel slope [22]. The first limiting case is when diffusion of a reactant species from a reservoir at the face of the electrode dominates the current distribution within the electrode. The second limiting case is when a nonuniform current distribution results because of ohmic losses in one phase of the electrode, either the electrolyte or the solid matrix. This latter case may also be thought of as mass-transport control, since a limited flux of either ions in the solution or electrons in the matrix is the source of these ohmic losses. A excellent summary of this work for flooded-porous electrodes has been provided by Newman and Tiedemann [22].

The first limiting case given above has also been extensively treated with GDE's. However, despite the fact that previous fuel-cell models have shown that ohmic losses in the electrolyte within the GDE may be responsible for a major portion of the potential losses at moderate current densities [23], the second limiting case has generally been neglected by GDE models, except for the two references [10, 24] which are discussed below. It should be noted that in pressurized systems where the gas concentration is increased, this second limiting case is even more likely to be relevant, especially in systems which employ electrolytes with relatively low ionic conductivity or a matrix with a low electrical conductivity.

2.3.1 Ambient-Temperature Fuel-Cell Cathodes

The performance of ambient-temperature fuel cells operating on hydrogen fuel is dominated by the behavior of the cathode, because the ORR is much slower than the anodic oxidation of hydrogen. At any appreciable current density, the irreversible ORR follows Tafel kinetics. It is also well known that a double Tafel slope results when the cathode is controlled by both the kinetics of the ORR and the transport of oxygen. In this case, the cathode performance is still first order with respect to the concentration of oxygen [25], which is as expected since both the kinetics of the ORR and the transport of oxygen (either by liquid-phase diffusion of dissolved oxygen or by gas-phase diffusion of molecular oxygen) are first-order processes.

In ambient-temperature fuel cells, the gas-transport phase is typically provided by the hydrophobic PTFE, which prevents the electrolyte from completely flooding the void spaces of the porous matrix. The PTFE also serves as the binder for the small particles of supported electrocatalyst which comprise the solid matrix of these GDE's. The electrocatalyst in these cells is typically a noble metal (such as Pt or a Pt alloy), and the support (if any) is typically a high-surface-area carbon. Both of these materials provide high electrical conductivity, and therefore the transport of electrons is normally not a significant factor within the active layer of these electrodes. Therefore, it is the relative rates of the gas and ion transport compared to the electrochemical reactions which determine the current distributions within the electrodes, and ultimately the potential-current characteristics of these fuel cells.

A model developed for an oxygen cathode with an aqueous-carbonate electrolyte by Striebel *et al.* [10, 11], which includes the diffusion and migration of ions in the

solution phase, predicts that the double-Tafel-slope region exhibits half-order dependence on the oxygen partial pressure. This result was supported by experimental data. The mobility of the principal charge carrier in this buffered electrolyte, the bicarbonate ion, is much lower than that of hydroxyl ions or protons. Therefore, this system becomes controlled by ionic transport at relatively low current densities (lower than the current at which oxygen transport becomes limiting). Additionally, this limited ionic transport produces dramatic increases in the *p*H of the cathode, since the concentration of hydroxyl ions is small in this buffered electrolyte and the ORR in an alkaline medium produces hydroxyl ions. This also has a negative effect on the electrode performance, since the ORR is very *p*H sensitive.

Ross [24] also arrived at a half-order oxygen dependence for a fuel-cell cathode controlled by kinetics and ionic transport from perturbation-theory solutions of asymptotic approximations derived from a simple model. He also presented some data with phosphoric-acid cathodes which show "anomalous current ratios" which trend towards a half-order oxygen dependence. However, this work was never published in the open literature. It should also be noted here that Austin [26] derived, in a clear and concise manner, asymptotic solutions for these two limiting cases for a flooded-porous electrode. Although the geometry of the system he treated is different from a fuel-cell cathode, it is inconsequential for these two particular limiting cases. However, he did not emphasize the different reaction orders that result for these two cases.

2.3.1 Research Objectives of the Fuel-Cell Cathode Models

The purpose of the modeling portion of this work was to examine, with a mathematical model of a fuel-cell cathode, the two limiting cases outlined above, as well as the case where the cathode is controlled by all three factors – kinetics, oxygen transport, and ionic transport. Two separate models were developed, one for liquid-electrolyte cathodes and one for a cathode with a polymer electrolyte. The rigorous numerical solutions of these models has been supplemented with analytic asymptotic solutions, as well as a physical explanation of the results. How these results may be used as a diagnostic tool to analyze fuel-cell cathode data and optimize the performance of a GDE is also presented.

Chapter 3. Direct-Hydrocarbon Polymer-Electrolyte Fuel Cell

"Science is a cemetery of dead ideas." — Miguel de Unamuno

3.1 Experimental Procedures

The initial experimental approach was to build a complete PEFC and check the performance of this test cell by comparing its hydrogen/oxygen performance with previous results reported in the literature. Although the performance of a PEFC operating on hydrogen is dominated by the cathode, and this work is concerned primarily with the anode, it was felt that the challenge presented by the sluggish ORR would be somewhat analogous to the task of oxidizing hydrocarbons at the anode. Therefore, satisfactory complete-cell results were considered to be an adequate indicator that the GDE structure was adequately optimized to provide a fair test of the anodic oxidation of hydrocarbons.

The test cell used in this work was based on the design developed at LANL [27] with two fundamental differences. The active cell area was 20 cm^2 (*vs.* the 5-cm^2 cells typically used at LANL), and the cell was completely encased in Teflon blocks to eliminate the gas leaks that are prevalent in the LANL cells. These two changes appeared to introduce some adverse effects which had to be initially overcome. Preparing good electrodes with a larger active area presents a greater challenge, probably because of greater nonuniformity in the active layer and in the bond formed with the electrolyte membrane. LANL has also experienced some difficulties in obtaining consistent results with their larger cells (50-cm^2 active area) [28]. (The 20-cm^2 size was chosen to ensure an adequate flow rate of exit gases from the anode to be analyzed by a gas chromatograph

and to reduce the amount of error involved in measuring the relatively low current densities expected with hydrocarbons.) This essentially leak-proof design adversely affected the water-management problem, especially at high current densities where flooding of the cell appeared to be a more common occurrence than in the LANL cells. The flow rates employed in this work (no more than 2 to 4 times stoichiometric) were also lower than what is commonly used at LANL.

3.1.1 Membrane Electrode Assembly (MEA)

Although a fuel cell appears to be a very simple device on a macroscopic scale, it is very complex on a molecular level. As explained in Section 2.3, all of the species required for the heterogeneous electrochemical reaction must be present at the electrocatalyst sites in order for these sites to be active. Therefore, the performance of a fuel cell is extremely sensitive to the microstructure of the electrodes.

The polymer electrolyte must be in intimate contact with the catalyst in the active layer of an effective PEFC electrode. This is usually accomplished by utilizing the ionomer in a liquid form and either painting this solution onto prefabricated electrodes [27] or mixing the solution with supported catalyst to form an "ink" and casting this ink onto a suitable support, or directly onto the electrolyte membrane, to form a very thin active layer [29-32]. Two electrodes, an anode and a cathode, are then hot pressed to the polymer-electrolyte membrane to form a membrane electrode assembly (MEA).

During the initial stages of this work, a wide variety of MEA preparation procedures was explored, including all of the methods described in the above references, as well as various combinations of these techniques. However, the most successful and

consistent (especially with the relatively high catalyst loadings used here, >0.25 mg Pt/cm^2), results were obtained using a commercially available carbon cloth GDE (E-TEK, Inc.) and painting a 5 w/o Nafion® 117 solution in a mixture of lower aliphatic alcohols and 10% water (Aldrich Chemical Co.) onto the active layers of these electrodes, as described in detail by researchers at LANL [27]. The E-TEK electrodes used in this work typically contained 20 to 40 w/o Pt on Vulcan XC-72 Carbon with a 0.35 to 2.0 mg Pt/cm^2 loading. Nafion® loadings in the electrodes were in the range of 0.5 to 5 mg/cm^2, and a Nafion® loading of approximately one-half the weight of the Pt and carbon in the active layer was found to be typically optimum (*i.e.*, for an electrode with 20 w/o Pt on C at a loading of 0.35 mg Pt/cm^2, the Nafion® loading was approx. 0.875 mg/cm^2). Three different membranes were used: Nafion® 112, Nafion® 115, and Nafion® 117 (du Pont), and the thicknesses in the dry state were 50, 125, and 175 μm, respectively.

The MEA's were formed by placing two 20-cm^2 Nafion®-doped GDEs on either side of an approximately 40-cm^2 piece of Nafion® membrane. This assembly is inserted into a hot press (Carver, Inc.) with the two platens set to a temperature of 100° C, and a light load is applied until the press heats up to 125° C. The assembly is then pressed at 60 to 80 atm. for 60 to 90 s to obtain a good bond between the membrane and the electrodes.

3.1.2 Cell Design and Auxiliary Apparatus

A single-cell test PEFC was designed and fabricated to accommodate the 20-cm^2 electrodes. A schematic diagram of this cell is shown in Fig. 3-1. Machined graphite blocks, having serpentine channels on one side, facilitate the distribution of humidified reactant gases to the GDE's on the MEA, as well as providing current collection from the

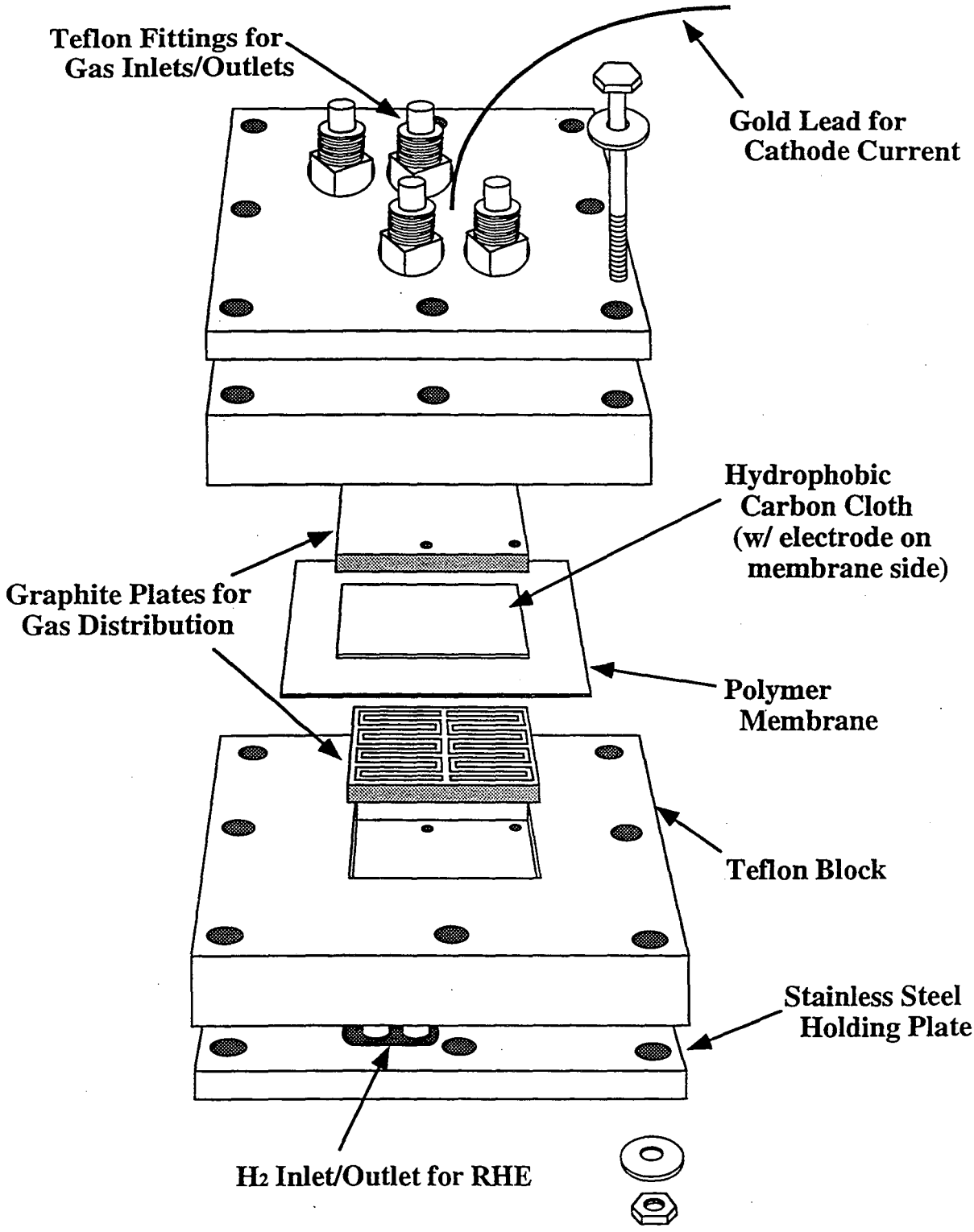

Figure 3-1. Schematic Diagram of a Polymer Electrolyte Fuel Cell (PEFC) for laboratory experiments.

electrodes. Two channel designs were tested, a single channel and a dual channel (shown). Thin pieces of gold foil (not shown in Fig. 3-1) were placed behind each of the graphite blocks and bonded to the gold wire leads to minimize contact resistance. PTFE blocks, with recesses for the graphite blocks, provided sealing on bolting the cell components together, which included stainless-steel endplates for good compression of the cell. Gases flowed in and out of the cell through PTFE tubes inserted into the PTFE fittings which were in turn threaded into the PTFE blocks.

A hydrogen reference electrode (RHE), not shown in Fig. 3-1, was provided on the anode side of the cell by bonding a small piece of E-TEK electrode (*ca.* 1 cm^2) to the membrane and equilibrating it with H_2 via the small inlet and outlet located in this position (which is shown in Fig. 3-1). It was anticipated that some hydrogen from the RHE may diffuse to the anode, which would not affect the cell tests with hydrogen feed but was clearly unacceptable with the hydrocarbons. Therefore, when testing hydrocarbons, half-cell data were obtained by flowing humidified nitrogen across the cathode and evolving hydrogen at the cathode. At the low current densities obtained with these fuels, the activation overpotential of hydrogen evolution was assumed to be negligible; this assumption was tested by comparing the measurements described above with the results obtained by subtracting the cathode polarization for a given cell (measured during the hydrogen/oxygen test) from the data for the complete hydrocarbon fuel cell. The agreement was within experimental error (10 to 20 mV, depending on the fuel). The test cell was always purged with nitrogen, and current was passed under short-circuit conditions until the current was nil, prior to changing gases on the electrodes.

The PEFC was placed inside a large convection oven (Associated Testing Laboratories Inc., Model SK-3105) for operation at various selected temperatures. The reactant gases were pre-humidified by sparging them through columns of water (*ca.* 0.3 m high) in glass vessels, located just outside the oven and wrapped with heating tape. The temperature of the humidification vessels could be monitored and controlled by two temperature controllers (Oven Industries, Inc.). The temperature of the anode humidifier was typically maintained approximately at, or 5° C higher than, the oven temperature whereas the cathode humidifier was kept at approximately oven temperature, or 5 to 10° C below this temperature at high current densities (> 400 mA/cm^2). (Note that these humidification levels are lower than those recommended by LANL [27])

All experiments were conducted at ambient pressure. After passing through the cell, the exit gases were purged into polypropylene containers filled with water to provide a modest amount of back pressure. The flow rates of the reactant gases were controlled and monitored by mass-flow meters (Omega Engineering, Inc.). Pure (>99.0%) hydrogen and oxygen were typically fed at approximately 1.2 to 2 times their stoichiometric rates. The hydrocarbon fuels and air were fed at 2 to 4 times their stoichiometric rates. Seven hydrocarbon gases (Airgas, C. P. grade) were tested as fuels: methane, ethane, propane, n-butane, ethylene, propylene, and iso-butlyene. All were certified to be at least 99.0% chemically pure, with less than 10 ppm of carbon monoxide and 100 ppm of hydrogen sulfide.

After allowing at least 24 h to condition a new MEA with pure hydrogen and oxygen at low current densities (<100 mA/cm^2) and a temperature of 50° C, the performance characteristics of a cell were determined. Galvanostatic experiments were

controlled by a Hokuto-Denko Potentiostat/Galvanostat (Model HA-320G) and recorded by hand using digital multimeters (Keithley, Model 173A) which were connected to the gold-lead wires on the test cell. Three potentials were normally recorded: the cell potential, the anode *vs.* RHE, and the cathode *vs.* RHE. Additionally, a strip chart recorder plotted the cell potential as a function of time to determine when it reached a steady value. Ohmic (*iR*) correction measurements were made via the current-interrupt method using a mercury-wetted relay switch. A digital oscilloscope (Nicolet Instrument Co., Model 2090-IIIA) was used to determine the *iR*-free values. The potential drop attributed to purely ohmic resistance was that measured approximately 10 μs following the interruption of current.

3.2 Results and Discussion

The performance curve (including ohmic losses) obtained with a test PEFC operating on hydrogen and oxygen is depicted in Fig. 3-2, and is compared with two previous results reported in the literature [27,32]. The MEA of this test cell was prepared in the same manner as the LANL cell [27], and therefore the similarity in performance is not surprising. The MEA in the Matsushita cell was prepared by a different "colloidal solution" process, which the authors claim increases the catalyst utilization and simplifies the preparation of the MEA [32]. However, this method does not appear to produce results better than the LANL method, despite the higher catalyst loadings and the thinner membrane used in this cell. Note that the catalyst loadings of all three cells in this figure are quite similar. Although the catalyst loadings used in the direct-hydrocarbon test cells

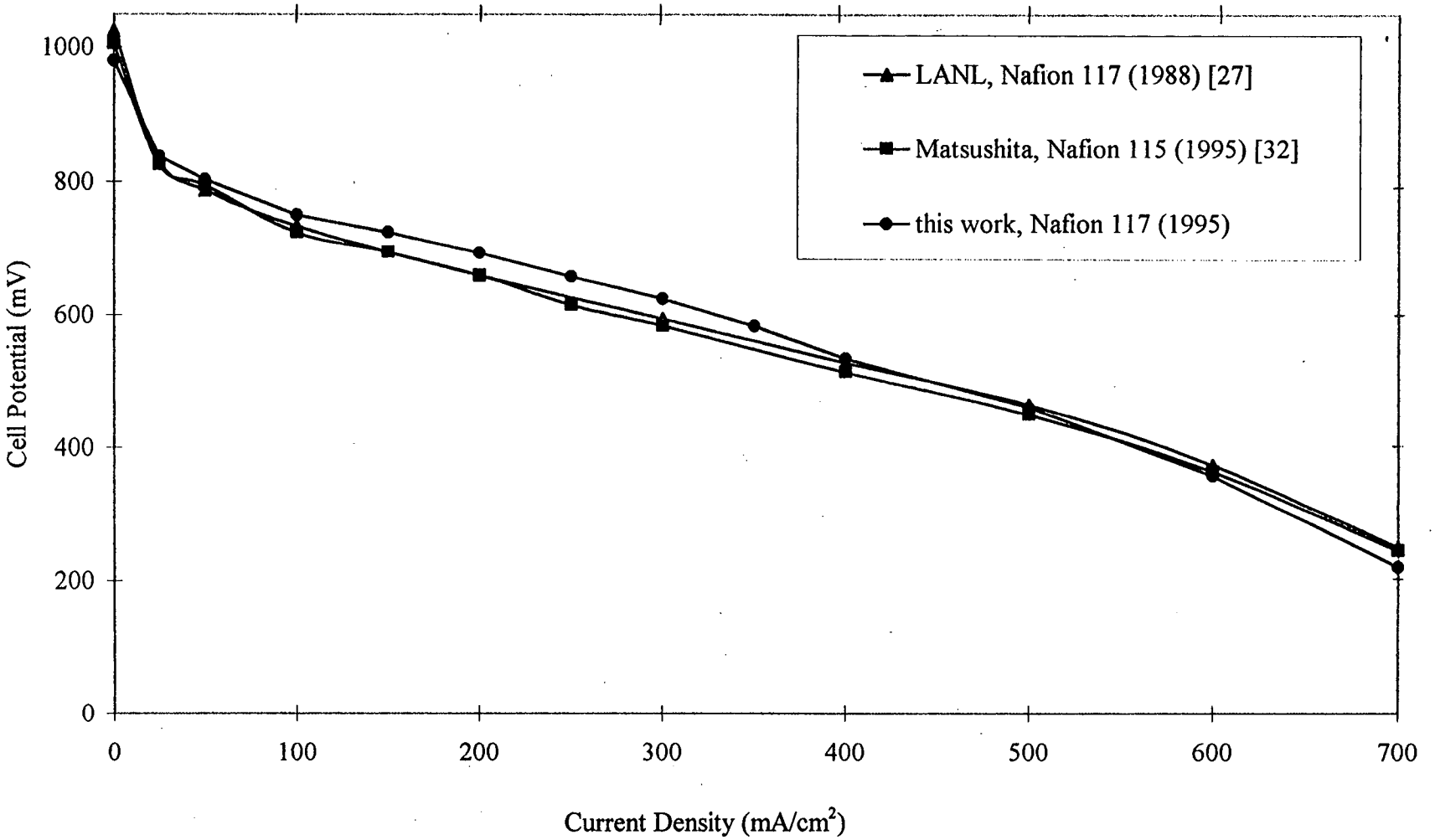

Figure 3-2. Performance curves for three PEFC's operating on hydrogen and oxygen at 1 atm. and 50° C. Catalyst loadings/electrode: LANL and this work (both 20 w/o Pt on C) = 0.35 mg Pt/cm^2; Matsushita (25 w/o Pt on C) = 0.50 mg Pt/cm^2.

were considerably higher, the hydrogen current density, at a given cell/electrode potential, was also typically higher by an amount approximately proportional to the increase in the reported Pt surface area, as expected (at least for current densities of less than 100 mA/cm^2 and catalyst loadings less than 1.5 mg/cm^2, where mass transport effects are not too significant).

Fig. 3-3 compares the performance of a test cell operating on propane and oxygen with an early PEFC, from the General Electric (GE) Company Research Laboratory in Schenectady, New York [33], operating under similar conditions. GE researchers referred to these early PEFC's, which utilized hydrocarbon-based polymers, as "Ion-Exchange-Membrane Fuel Cells" (IEMFC's). The performance of the Nafion® PEFC is clearly superior to the IEMFC, despite the order-of-magnitude lower catalyst loadings employed in this work. It should be noted, however, that these GE cells did not use catalyst layers impregnated with the polymer electrolyte, and therefore the catalyst utilization was probably very poor compared to the state-of-the-art MEA's used in this work, which were demonstrated to improve the Pt utilization by an order of magnitude on hydrogen and oxygen as well [27]. These IEMFC's also used Pt black as a catalyst, which has a lower specific surface area (*ca.* 28 m^2/g) and is more prone to sintering at high electrode fabrication or operating temperatures than the supported catalyst employed here (40 w/o Pt on C, reported to have *ca.* 72 m^2/g [34]). In addition, some of the increase in performance may be due to the superior ORR kinetics of Nafion® relative to the reinforced sulfonated phenolformaldehyde casting resin used in this IEMFC. It is not possible to compare just the anode performance, since half-cell data were not reported for the IEMFC.

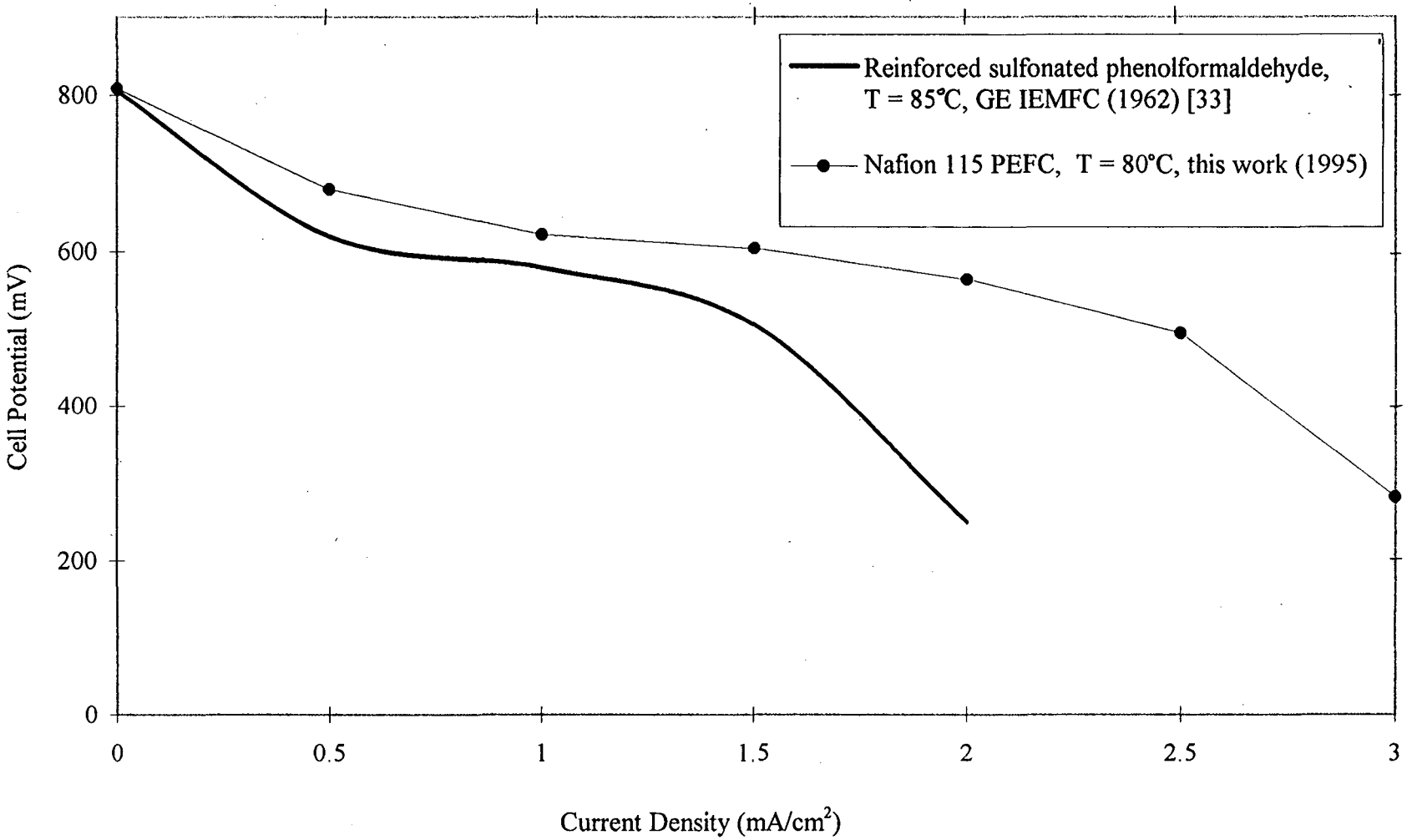

Figure 3-3. Performance curves for two full cells operating on propane and oxygen at 1 atm. Catalyst loadings/electrode: GE IEMFC = 18 mg Pt black/cm^2; this work (40 w/o Pt on C) = 1.5 mg Pt/cm^2.

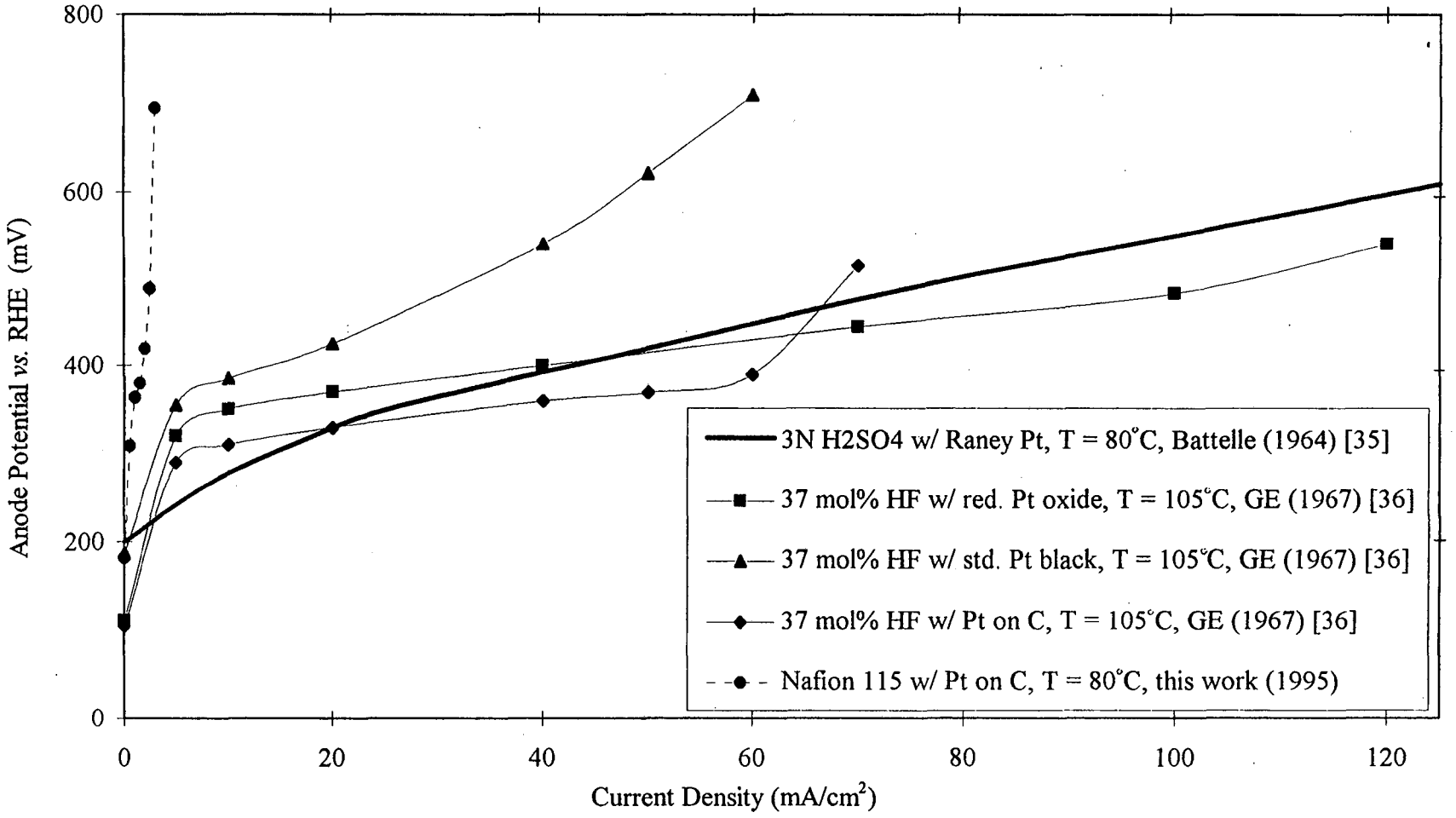

Figure 3-4. Performance curves (*iR*-free) for half cells operating on propane at 1 atm. Catalyst loadings: Battelle Institute = 180 mg Raney Pt/cm^2; GE anodes: standard Pt Black and reduced commercial Pt oxide both = 25 mg Pt/cm^2, Pt on C (unspecified w/o) = 7.14 mg Pt/cm^2; this work (40 w/o Pt on C) = 1.5 mg Pt/cm^2.

When the anode performance (*iR*-free) of the PEFC on propane is compared with similar half-cell data reported for liquid electrolytes, as shown in Fig. 3-4, the results are not so encouraging. Once again, one must consider the large differences in catalyst loadings among the cells compared here; however even after correcting for this difference, Nafion® does not appear to be a superior electrolyte for the oxidation of hydrocarbons relative to strong acids such as HF, as shown by Table 3-1. Ideally, one should compare the performance based on the activity per unit surface area of electrocatalyst. (The importance of the specific area is readily apparent when one compares the specific activity of the two Pt blacks prepared by different methods in the HF electrolyte; and another preparation of reduced PtO_2, not shown in Fig. 3-4, produced ~ 3.2 mA/mg of Pt at the same potential and temperature [36].) Unfortunately, the specific area of the Pt catalyst used in this previous work was not determined. However, if one uses the specific areas stated above for this work and the standard Pt black, then a rough comparison can be made on this basis, as shown in the last column of Table 3-1. (Since the w/o of Pt on carbon was not reported for the supported Pt in HF, the Pt surface area cannot be estimated for this case.)

One might object to the previous comparison of data at two different operating temperatures. Fortunately, an Arrhenius plot for the GE 37mol% HF anode from 30 to 105° C is reported elsewhere [20]. With this information we can estimate the specific activity of this system with the standard Pt black to be approx. 1.3 $\mu A/cm^2$ of Pt (0.36 mA/mg of Pt) at 0.4 V and 80° C. The effect of temperature will be discussed in greater detail in the next section.

Table 3-1. Comparison of propane anode performances shown in Fig. 3-4.

Electrolyte, T (°C) Pt type, loading (mg/cm^2)	i @ 0.4 V *vs.* RHE (mA/cm^2)	i @ 0.4 V *vs.* RHE (mA/mg)	Pt Surface Area [34] (m^2/g)	i @ 0.4 V *vs.* RHE ($\mu A/cm^2$ of Pt)
3N H_2SO_4, 80 Raney, 180	43	0.24	N/A	N/A
37 mol% HF, 105 [36] reduced oxide, 25	40	1.6	N/A	N/A
37 mol% HF, 105 [36] standard black, 25	15	0.6	28	1.7
37 mol% HF, 105 [36] supported on C, 7.14	60	8.4	N/A	N/A
Nafion® 115, 80 supported on C, 1.5	1.8	1.2	72	2.1

Finally, it should be noted that preparing an effective MEA with a relatively high catalyst loading is difficult. The "ink" methods developed at LANL [29-31] appear to be best suited for the preparation of very thin catalyst layers (supported catalyst loadings of less than 0.25 mg Pt/cm^2); it was found to be very difficult to form robust, well-bonded, and thick catalyst layers in this manner. The MEA fabrication method used in this work, namely impregnating prefabricated GDE's with Nafion® solution [27], also has its limitations. The solution will penetrate the GDE only to a limited distance, and therefore may

not completely wet the active layer, especially for electrodes with very high loadings of supported catalyst [37]. This catalyst utilization problem is of course not limited to PEFC's; it becomes a critical factor for all GDE's at current densities where mass transport becomes limiting, which is a strong function of the structure of the electrode. Note that the performance of the supported Pt catalyst used in the GE anode [36], shown in Fig. 3-4, shows evidence of mass-transport limitations at just 60 mA/cm^2; although the non-supported Pt catalysts (with higher loadings) do not appear to be significantly limited by mass transport. Even if one could construct a PEFC anode with a thick active layer of supported catalyst that would effectively utilize all of the Pt, it is doubtful that the results would be much better than what was obtained previously with liquid electrolytes. Such low-power-density fuel cells, with high Pt loadings, are not of practical interest.

The other hydrocarbons, listed in Section 3.1.2, were also tested as fuels in the PEFC; however the anode performance in all cases was inferior to that obtained with propane and was in general agreement with the trend found in the previous work [20] (*i.e.*, propane > ethane > n-butane > methane, ethylene, propylene, and iso-butlylene – the performance of the last four gases was so low that it was difficult to determine any difference).

It is interesting to speculate about why the performance of a direct-hydrocarbon PEFC was not significantly better than early results obtained with liquid-acid electrolytes, as expected. The first factor to consider is that competitive anion adsorption at the anode is not so important as at the cathode because of the more negative potentials at this electrode. Nevertheless, the previous results with various liquid electrolytes certainly

seem to indicate that this is an important factor, especially at the high overpotentials required to obtain appreciable reaction rates with hydrocarbons [20]. However, another important factor to consider is the difference in solubility of the reactants in these different electrolytes. First, since hydrocarbons are relatively nonpolar, their solubility in polar solutions (such as electrolytes) is extremely low. On the other hand, alkenes (and to lesser degree alkanes) are weak Lewis bases, and it is reasonable to assume that they will be more soluble in stronger acids [38, 39], and the limited data available on hydrocarbon gas solubility in acids does indeed support this general trend. In fact, the solubility of alkanes in aqueous acids is several orders-of-magnitude higher than in pure water [40]. Therefore, the strong acid electrolytes, which generally have the most weakly adsorbed anions (and were found to be the best liquid electrolytes [20]), also would be expected to have high hydrocarbon solubilities relative to weak acids.

Although hydrated Nafion® is a strong acid, the chemical environment of this electrolyte is much different from that in a free acid. For example, it has been shown by infrared spectral studies that water in Nafion® is much less strongly hydrogen-bonded than water in aqueous salt solutions at the same temperature [41]. Therefore, these water molecules are less likely to associate with each other or to solvate other molecules possessing accessible electronegative moieties. The explanation for this phenomenon may be that the space-charge regions in Nafion® are confined to a relatively thin shell (approximately equal to the Debye length) near the wall of the hydrophobic clusters within this polymer, and therefore the bulk of the water is shielded from the charges on the ions [42].

It should be emphasized that the above is purely speculation; the solubility of the hydrocarbons in hydrated Nafion® was not measured. However, the solubility of oxygen in a wide variety of electrolytes, including hydrated Nafion®, has been determined. It should be pointed out here that the solubility of oxygen in these electrolytes, which has been conveniently tabulated by Kinoshita [43], shows the opposite trend of hydrocarbons, it is lower in acids (~ $5x10^{-5}$ M in 98% H_3PO_4 and ~ $5x10^{-4}$ M in 70% H_2SO_4, both at 298° K) than it is in pure water (~$1x10^{-3}$ M at 298° K) and is quite high in hydrated Nafion® (~ $3x10^{-3}$ M at 298° K). Since the ORR is first order with respect to the concentration of oxygen in aqueous electrolytes [44], the difference in reactant gas solubility plays a significant role in determining which electrolyte provides the best ORR kinetics, in addition to the role of competitive anion adsorption.

3.3 Conclusions and Recommendations

Further work on direct-hydrocarbon PEFC's does not appear justified at this time. Extremely poor electrocatalytic activity remains the main barrier to the possibility of a practical low-temperature direct-hydrocarbon fuel cell. Despite our expectations that the PEFC performance would be better than previous work with strong acid electrolytes, due to reduced competitive anion adsorption with the polymer electrolyte and other factors, the performance obtained with the Nafion® membrane appeared to be similar to these previous results.

The results obtained with Pt as the electrocatalyst presents a no-win situation: to get higher current densities requires thick catalyst layers, and thicker catalyst layers are less effective at higher current densities. The very thick catalyst layers required almost

certainly preclude the use of supported catalysts due to the relatively low solubility of hydrocarbon fuels in aqueous electrolytes and the attendant mass-transport considerations. A better electrocatalyst than Pt for the anodic oxidation of hydrocarbons is not known at this time. The possibilities are also fairly limited due to the requirement of electrochemical stability. Pt-Ru alloys, which show enhanced activity for the anodic oxidation of methanol and CO compared to Pt [45, 46], do not appear to offer improved activity with hydrocarbons [20].

Even if an improved electrocatalyst for the anodic oxidation of hydrocarbons is identified, some fundamental studies would appear justified before attempting to build another direct-hydrocarbon fuel cell. The first would be to study the kinetics of the electrooxidation of hydrocarbons on well-characterized electrodes in the electrolytes of interest. One goal of this work would be to determine what is the reaction order with respect to the hydrocarbon partial pressure. If the current density at a given overpotential is proportional to the hydrocarbon partial pressure, as expected for the weakly adsorbed alkanes [20], then another important factor to investigate would be the solubility of these gases in the electrolytes of interest. With this approach, the most-promising electrolytes (and electrocatalyts) may be identified before constructing GDE's, which are not only difficult to optimize for a given system but also obscure these fundamental factors with complex mass-transport limitations.

Finally, it is clear from the previous work [20] that the performance of a direct-hydrocarbon fuel cell can be maximized by operating the cell at the highest temperature possible. Of course there are limitations on cell-operating temperatures, caused by the boiling points of the electrolytes, corrosion problems, electrode-structure degradation, and

electrocatalyst sintering. In the case of a PEFC, the temperature is primarily limited by the need to maintain the membrane in a hydrated state in order to achieve acceptable ionic conductivity. Raising the operating temperature of the PEFC to improve the sluggish hydrocarbon kinetics was considered; however this would also require raising the pressure to operate at greater than 100° C. At the low power densities involved here, this does not appear to be a practical alternative, due to the increased system complexity and cost, as well as the "parasitic" power required to operate an air compressor. Therefore, the most promising electrolyte may simply be that which can operate at the highest temperature at atmospheric pressure with minimal operating problems. Especially since the various alkanes of interest are not very sensitive to temperature – the overall activation energy for hydrocarbon oxidation in acid-electrolyte fuel cells was determined to be consistently in the range of 60 to 84 kJ/mol for a variety of these fuels in liquid electrolytes between room temperature and 200° C [20]. The results of the present work also yield a value in this range for propane with Nafion® from 25 to 80° C. Although the activation energy for this system cannot be projected beyond this temperature range, the similarity of the results is consistent with the idea that the rate-determining step is the same in these different electrolytes, and one might reasonably expect that it would remain so up to the temperatures previously investigated with liquid electrolytes.

Chapter 4. Theoretical Models of Fuel-Cell Cathodes

".... in so far as mathematics is about reality, it is not certain, and in so far as it is certain, it is not about reality." — Albert Einstein

4.1 Model Development

A porous electrode is a very complicated structure which is difficult to characterize on a microscopic level. One approach to this problem is porous-electrode theory [22], which employs a macroscopic model that accounts for the essential features of a porous electrode without going into exact geometric detail; this method has been used to treat a wide variety of flooded-porous electrodes. A GDE, such as a fuel-cell cathode, adds an additional degree of complexity to the problem since a third phase must be accounted for and this requires a model with dual porosity, one for the gas phase and one for the electrolyte, as well as boundary conditions between each of the phases. Since porous-electrode theory considers the electrode as a continuum, the boundary conditions must apply throughout the volume, and the problem becomes quite complex. One way to simplify this problem is to specify the size of the porous solid particles, and this is the basis of the flooded-agglomerate model. Although the size of an agglomerate particle may be somewhat uncertain (since this parameter may vary with position and be difficult to measure), the flooded-agglomerate model gives a good account of the physical processes involved, and the simplification that accompanies this approach allows one to derive instructive results. It should be recognized that the flooded-agglomerate model, when executed correctly, is essentially a discretized version of porous-electrode theory.

The goal of this work was to treat fuel-cell cathodes with a general model that would be applicable to common low-temperature systems. This includes the AFC (typically with a KOH electrolyte), the phosphoric-acid fuel cell (PAFC), and the PEFC. In each of these systems the ORR can be well represented by Tafel kinetics. Yet, the PEFC is substantially different from its liquid-electrolyte counterparts, and therefore a separate model was developed for this system. These two models, and the results, will be presented in separate sections of this thesis. However, the results of these two models also complement one another, and this feature will be discussed in the conclusions section of this chapter.

These models emphasize two important limiting cases: *i*) kinetics and oxygen transport are controlling the rate of the reaction in the GDE, and *ii*) control by kinetics and ionic transport. The case where the cathode behavior is simultaneously controlled by all three of these factors is also considered.

4.1.1 Liquid-Electrolyte Model

For this study, we have chosen to represent a fuel-cell cathode employing a liquid electrolyte with a flooded-agglomerate model. The flooded-agglomerate concept was first introduced by Giner and Hunter [25], who used a series of flooded-cylindrical agglomerates connected by hydrophobic gas pores to describe the catalyst layer of a modern PTFE-bonded GDE, and they showed that their model predicted a Tafel slope twice the

normal Tafel slope* due to mass-transfer limitations of oxygen in the electrolyte of a fuel-cell cathode at higher current densities. Iczkowski and Cutlip [23] also used a similar model, with spherical agglomerates, which included the diffusion of oxygen in the hydrophobic gas pores as well as in the solution phase. However, these previous models employed Ohm's law to treat ionic conduction in the electrolyte. Ohm's law is not applicable when concentration gradients exist, as was pointed out by Ross [47]; he also emphasized that the *p*H dependence of the ORR should be included as well. Consequently, these previous models are strictly valid only when the electrolyte concentration is uniform across the catalyst layer. Therefore, in this model we account for the effects of ionic migration and diffusion in the solution phase.

A schematic diagram of the model is presented in Fig. 4-1. We assume that the spherical agglomerates, which represent the carbon-supported catalyst particles flooded with electrolyte, have a small diameter compared to the thickness of the active layer. We also assume that the electrolyte composition is uniform within these small individual agglomerates. Therefore, if we neglect any ohmic losses within these small carbon particles, the potential within each agglomerate is constant, and we need only consider the diffusion and reaction of oxygen within the spherical agglomerates:

$$\mathscr{D}_o \frac{1}{r^2}\frac{\partial}{\partial r}\left(r^2 \frac{\partial c_o}{\partial r}\right) = - R_{ORR} \qquad (4\text{-}1)$$

---

* The normal Tafel slope *b* referred to herein is a strictly empirical one, what is sometimes refered to as the "nonkinetic" or "apparent" Tafel slope. It is defined as the initial slope of the straight-line portion of a polarization curve when plotted on a semi-logarithmic Tafel plot (*i.e.*, $b = -\partial V/\partial \log i$ for this cathodic reaction), at a potential where the complications arising from oxides on the surface are not especially significant (typically defined, for a Pt electrocatalyst, as below 0.8 V *vs.* RHE in the same solution [44]). Such a definition of *b* may include additional effects besides charge-transfer kinetics.

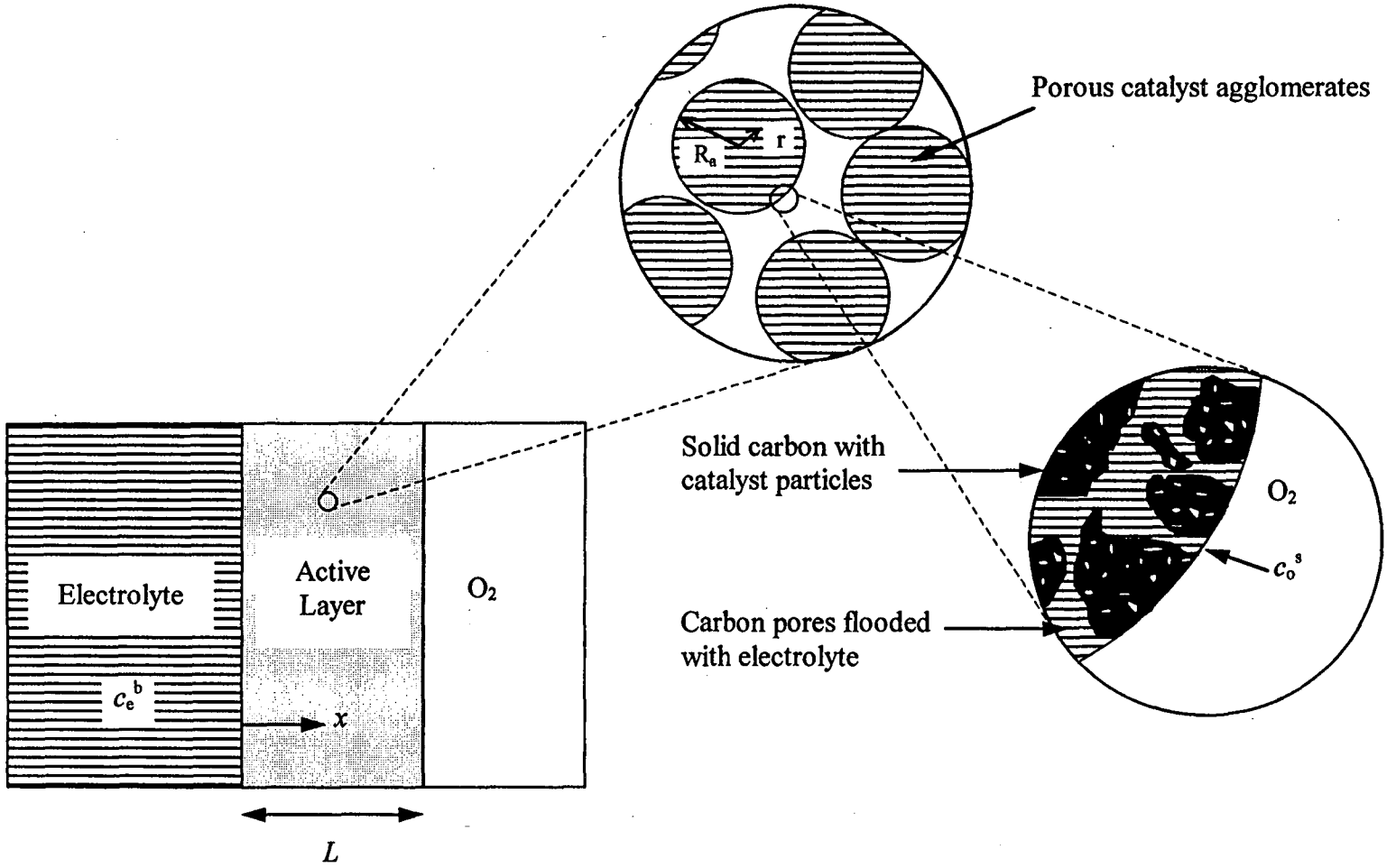

Figure 4-1. Schematic Diagram of Flooded-Agglomerate, Liquid-Electrolyte Model.

Here $\mathscr{D}_o$ is the effective diffusivity of oxygen in the porous agglomerate, which may be defined as $\mathscr{D}_o = D_o(\varepsilon_a/\tau_a)$, and is assumed to be a constant. The two boundary conditions for Eqn. 4-1 are set by (*i*) assuming that the concentration of oxygen is uniform in the relatively large PTFE-formed gas pores (*i.e.*, neglecting gas-phase diffusion), and (*ii*) noting that the flux of oxygen at the center of an agglomerate is zero:

$$\begin{aligned} &(i) \quad \text{at} \quad r = R_a, \quad c_o = c_o^{\,s} \\ &(ii) \quad \text{at} \quad r = 0, \quad \nabla c_o = 0 \end{aligned} \tag{4-2}$$

The ORR is assumed to exhibit Tafel kinetics and be first-order in O_2 concentration for the electrolytes of interest [44]:

$$-R_{ORR} = \frac{a_a i_n}{n\mathrm{F}} = \frac{a_a i_o}{n\mathrm{F}} \exp\left(-2.3\eta/b\right) = a_a k c_o \exp\left(-2.3\eta/b\right) \tag{4-3}$$

where η is the local overpotential, which we consider to be constant within each agglomerate, but which varies with position x in the active layer. The local overpotential is defined as $\eta = \Phi_1 - \Phi_2 - U^\theta$, where Φ_1 is the potential of the solid phase, Φ_2 is the potential of solution measured by a given reference electrode. This reference electrode, perhaps imaginary, is located within the active layer or just outside the agglomerate; and U^θ is the cell potential of the oxygen electrode relative to the given reference electrode.

An analytic solution to Eqn. 4-1, for a first-order reaction with the given boundary conditions, is provided by Bird, Stewart, and Lightfoot [48]:

$$c_o = c_o^{\,s} \frac{R_a}{r} \frac{\sinh(\phi r)}{\sinh(\phi R_a)} \tag{4-4}$$

in which ϕR_a is a dimensionless parameter, commonly known as the Thiele modulus; in this case:

$$\phi R_a = \sqrt{\frac{a_a k}{\mathcal{D}_o}} R_a \exp(-2.3\eta/2b) \tag{4-5}$$

We can now use Eqn. 4-4 to calculate the molar flux of oxygen, N_o, into a single agglomerate, which is proportional to the current produced in an agglomerate by Faraday's law:

$$I_a = n\mathrm{F}\left(4\pi R_a^2\right) N_o = -nF\left(4\pi R_a^2\right) \mathcal{D}_o \left.\frac{\partial c_o}{\partial r}\right|_{r=R}$$

$$= -4\,\pi\, n\mathrm{F}\mathcal{D}_o\, R_a\, c_o^s \left[\phi R_a \coth(\phi R_a) - 1\right] \tag{4-6}$$

This last result is also provided by Bird *et al.* [48].

We now have an expression for the rate of the reaction in each agglomerate particle in terms of the overpotential η that exists in each of the agglomerates. This overpotential will vary across the thickness of the active layer, since Φ_2 is not a constant in this region due to the potential gradient that forms in the electrolyte when current is passed. (We are neglecting ohmic losses in the carbon matrix, and therefore assume that the solid-phase potential, Φ_1, is a constant.)

We use dilute-solution theory expressions to treat the liquid phase, which is not strictly valid for concentrated fuel-cell electrolytes. However, it gives a good account of the physical processes involved without excessive complication. The fuel-cell systems of interest may be treated as binary electrolytes. If we assume that there is no convection

within the active layer and concentration variations in only one direction, x, then the cation and anion flux densities in a porous medium may be written as [22]:

$$\frac{N_+}{\varepsilon_a} = \frac{i_2}{\varepsilon_a z_+ \mathrm{F}} = -z_+ u_+ \mathrm{F} \nu_+ c_e \frac{\partial \Phi_2}{\partial x} - D_+ \nu_+ \frac{\partial c_e}{\partial x} \tag{4-7}$$

$$\frac{N_-}{\varepsilon_a} = 0 = -z_- u_- \mathrm{F} \nu_- c_e \frac{\partial \Phi_2}{\partial x} - D_- \nu_- \frac{\partial c_e}{\partial x} \tag{4-8}$$

where $c_e = c_+/\nu_+ = c_-/\nu_-$. (Note that Eqns. 4-7 and 4-8 are written for an acid electrolyte, *i.e.*, we have assumed that only the cations react at the cathode. For an alkaline electrolyte, the cation flux density would be set equal to zero, which would result in the "+" and "-" subscripts being interchanged in the following equations.) We can combine these cation and anion flux density expressions to eliminate the potential gradient as shown by Newman [49]:

$$\frac{i_2}{z_+ \nu_+ \mathrm{F}} = -\frac{\varepsilon_a D_e}{1 - t_+} \frac{\partial c_e}{\partial x} \tag{4-9}$$

where

$$D_e = \frac{z_+ u_+ D_- - z_- u_- D_+}{z_+ u_+ - z_- u_-} \quad \text{and} \quad t_+ = 1 - t_- = \frac{z_+ u_+}{z_+ u_+ - z_- u_-}$$

Note that the ionic diffusion coefficients and the mobilities also require a correction for the tortuosity of the agglomerate pores (a porosity factor has already been taken out), and therefore we shall use an effective diffusivity of the binary electrolyte, $\mathcal{D}_e = D_e (\varepsilon_a/\tau_a)$, in Eqn 4-9.

Since all of the current carried by the ions in the solution phase, i_2, is converted to electronic current, i_1, at the catalyst sites within the agglomerates, we can relate the

gradient of the ionic current to the sum of the current produced by the agglomerates within the active layer, which allows us to combine the derivative of Eqn. 4-9 with the results of Eqn. 4-6:

$$\frac{\partial i_2}{\partial x} = -\frac{z_+ \nu_+ \mathrm{F} \mathscr{D}_e}{1-t_+} \frac{\partial^2 c_e}{\partial x^2} = \rho_a \, I_a = -4\pi n \mathrm{F} \mathscr{D}_o \rho_a R_a c_o^{\,s} \left[\phi R_a \coth(\phi R_a) - 1\right] \quad (4\text{-}10)$$

where ρ_a is the density of agglomerates in the active layer:

$$\rho_a = \frac{\text{number of agglomerates}}{\text{unit volume of electrode}} = \frac{3(1-\varepsilon_l)}{4\pi R_a^{\,3}} \quad (4\text{-}11)$$

We can then use Eqn. 4-8 along with the Nernst-Einstein relation, $D_i = RTu_i$, to define the gradient of the electrolyte potential:

$$\frac{\partial \Phi_2}{\partial x} = -\frac{RT}{z_- \mathrm{F} c_e} \frac{\partial c_e}{\partial x} \quad (4\text{-}12)$$

This expression may be integrated from $x = 0$ ($c_e = c_e^{\,b}$) to x:

$$\Phi_2 + U^\theta = -\frac{RT}{z_- \mathrm{F}} \ln\left(\frac{c_e}{c_e^{\,b}}\right) \quad (4\text{-}13)$$

where we have arbitrarily chosen to set $\Phi_2 = U^\theta$ at $x = 0$. Using this result in Eqn. 4-5 allows us to eliminate Φ_2, and U^θ, from the parameter ϕR_a. Additionally, we note here that the rate constant k varies with pH, and we may express this dependence explicitly as $k = k' (c_e/c_e^{\,b})^{\gamma_+}$. The result is:

$$\phi R_a = \sqrt{\frac{a_a k'}{\mathscr{D}_o}} \left(\frac{c_e}{c_e^{\,b}}\right)^{\frac{\gamma_+}{2}} R_a \exp\left[-\frac{2.3}{2b}\left(\Phi_1 + \frac{RT}{z_- \mathrm{F}} \ln\left(\frac{c_e}{c_e^{\,b}}\right)\right)\right] = \left(c_e^{\,*}\right)^\theta \exp(\psi/2) \quad (4\text{-}14)$$

where $\theta = \gamma_+/2 - 2.3RT/2bz_-\mathrm{F}$ is a dimensionless parameter, $c_e^{\,*}$ ($= c_e/c_e^{\,b}$) is the dimensionless electrolyte concentration, and ψ is a dimensionless potential:

$$\psi = -2.3\Phi_1/b + \ln\left(\frac{a_a k' R_a^{\,2}}{\mathscr{D}_o}\right) \tag{4-15}$$

The model then reduces to one dimensionless equation with one unknown, c_e^*:

$$\frac{\partial^2 c_e^*}{\partial x^{*2}} = P\left\{\left(c_e^*\right)^\theta \exp(\psi/2)\coth\left[\left(c_e^*\right)^\theta \exp(\psi/2)\right] - 1\right\} \tag{4-16}$$

with the boundary conditions,

$$\begin{aligned} &(i) \quad \text{at } x^* = 0, \quad c_e^* = 1 \\ &(ii) \quad \text{at } x^* = 1, \quad \frac{\partial c_e^*}{\partial x^*} = 0 \end{aligned} \tag{4-17}$$

where x^* ($= x/L$) is a dimensionless distance and P is a dimensionless parameter which contains the dissolved oxygen concentration in the electrolyte (which is assumed to be proportional to the partial pressure of oxygen according to Henry's Law, $c_o^s = H_o p_o$):

$$P = \frac{3n\left(1-t_+\right)\left(1-\varepsilon_l\right) L^2 D_o c_o^s}{z_+ \nu_+ R_a^{\,2} D_e c_e^b} \tag{4-18}$$

Not only is P proportional to the oxygen concentration for a given system, but more importantly, it is a measure of the relative rates of diffusion of dissolved oxygen and the mass transport of ions in the electrolyte. The ranges of P considered for the two liquid electrolytes of interest were chosen by order-of-magnitude estimates of three non-dimensional terms that make up this parameter, as shown in Table 4-1. The first term, which is composed of electrochemical parameters and a constant, is on the order of unity for both systems.

The second term is a ratio of the geometric parameters. The active layer thickness L of a PTFE-bonded GDE is typically less than 0.4 mm [50], and a range of 10^{-2} to 10^{-1}

Table 4-1. Order-of-magnitude estimates of the parameters for the liquid-electrolyte model, with $p_o \approx 0.1$ to 1 atm.

Fuel Cell Type	$\frac{3n(1-t_\pm)}{z_\pm \nu_\pm}$	$\frac{(1-\varepsilon_l)L^2}{R_a^2}$	$\frac{D_o c_o^s}{D_e c_e^b}$	P	θ	P_x
AFC ~ 30% KOH T ~ 60 to 80° C	~ – 1	~10^3 to 10^6	~10^{-7} to 10^{-5}	~ – 10^{-4} to – 10	– 0.25	– 0.44
PAFC ~ 98% H_3PO_4 T ~ 150 to 200° C	~ 1	~10^3 to 10^6	~10^{-5} to 10^{-3}	~10^{-2} to 10^3	0.75	0.27

was used for L. Pebler [51] measured an agglomerate radius of ~ 3×10^{-5} to 1×10^{-4} mm for PTFE-bonded carbon particles by a transmission electron microscopy examination.

The third term is a ratio of the diffusivity and solubility of oxygen relative to the diffusivity and concentration of the electrolyte. Note that this ratio will vary less with temperature and composition than the individual parameters which constitute it. However, this ratio varies dramatically between the two systems. This variation arises because phosphoric acid is a weak acid, is only partially dissociated, and polymerizes at the high concentrations utilized in PAFCs [52], whereas KOH is a strong base. $D_e c_e^b$ was

estimated to be ~ 10^{-7} mol/cm·s for KOH and ~ 10^{-8} for H_3PO_4 based on [53] and [54], respectively. On the other hand, $D_o c_o^s$ is about an order of magnitude higher in concentrated H_3PO_4 (~ 10^{-12} to 10^{-11} mol/cm·s·atm [55]) than in KOH (~ 10^{-13} to 10^{-12} [56]).

A second parameter, θ, must also be estimated for these two systems; this includes the Tafel slope b and the reaction order with respect to the pH. Many different values have been reported in the literature for these two parameters, and this is because the kinetics of the ORR on Pt, and other metals, is complicated by the changing oxidation state of the metal and the amount of oxides on the surface of the catalyst, especially at potentials near the open-circuit value. For this study, we are interested in the behavior at high current densities (high overpotentials), and therefore one should use the values reported for the so-called "high-current-density region" [57], where oxide coverage is minimal. This region is typically defined as potentials below 0.8 V *vs.* a RHE in the same solution [44]. Because of the complications arising from changes in kinetic mechanisms above this potential, which are not accounted for in this model, we should restrict the application of this model to potentials below this value and also define the normal Tafel slope in this potential range. At high current densities, the Tafel slope for the ORR in acid and alkaline solutions is approximately $2 \times 2.3RT/F$, and the reaction orders with respect to $[H^+]$ are 1 and 0, respectively [57]. Therefore, $\theta \approx -1/4$ for KOH; whereas for H_3PO_4 $\theta \approx 7/12$ assuming complete ionization, or more realistically, $\theta \approx 3/4$ assuming single ionization of this weak acid. (Note that both P and θ are negative for an alkaline

electrolyte, this is a reflection of the fact that the concentration gradient forms in the opposite direction for alkaline system vice an acid electrolyte.)

Eqn. 4-16 was solved numerically with BAND [58]; and the computer program is given in Appendix A.

4.1.2 Polymer-Electrolyte Model

There are two major differences between a PEFC GDE and the PTFE-bonded GDE's used in liquid-electrolyte fuel cells. First, in a polymer electrolyte, where the anions are bound to the polymer chain, a cation concentration gradient cannot form due to the requirements of electroneutrality (*i.e.*, c_+, and c_e, are constant). Secondly, in a state-of-the-art-PEFC GDE employing a perflourosulfonic acid (PFSA), such as Nafion®, there are typically only two phases present, namely the solid matrix and the polymer electrolyte. The addition of PTFE was found to be not necessary, since the PFSA polymer acts as binder and it also contains a flourocarbon backbone which provides a hydrophobic region for the transport of gases [29]. In this case the transport of both ions and gases occur only in the electrolyte phase* , and the continuum approach of porous-electrode theory appears to be well-suited for the geometry of these GDEs.

Although one can still imagine separate microscopic regions where gas-phase transport may be taking place (*e.g.*, the hydrophobic pores of the Nafion®), these regions are essentially identical both outside and within the porous solid particles, and therefore this type of a GDE has a structure similar to a flooded-porous electrode. The transport

---

* Once again, gas-phase mass-transport limitations are neglected in this model.

properties used are those which are measured for the PFSA membrane with appropriate correction factors for the porosity and the tortuosity of the catalyst layer. These properties are a strong function of the water content of the polymer [13, 59]. Although the variation in water content across these very thin catalyst layers may be negligible at a given operating condition, the water content may vary significantly with large changes in the current density for the same cell. Water transport is not included in this model. Water and thermal management of a PEFC has been treated extensively elsewhere [60].

A schematic diagram of the one-dimensional PEFC cathode model is presented in Fig. 4-2. Since the composition of the electrolyte in the catalyst layer is uniform, if one neglects water-content variations in this layer, then Ohm's law is valid for the electrolyte:

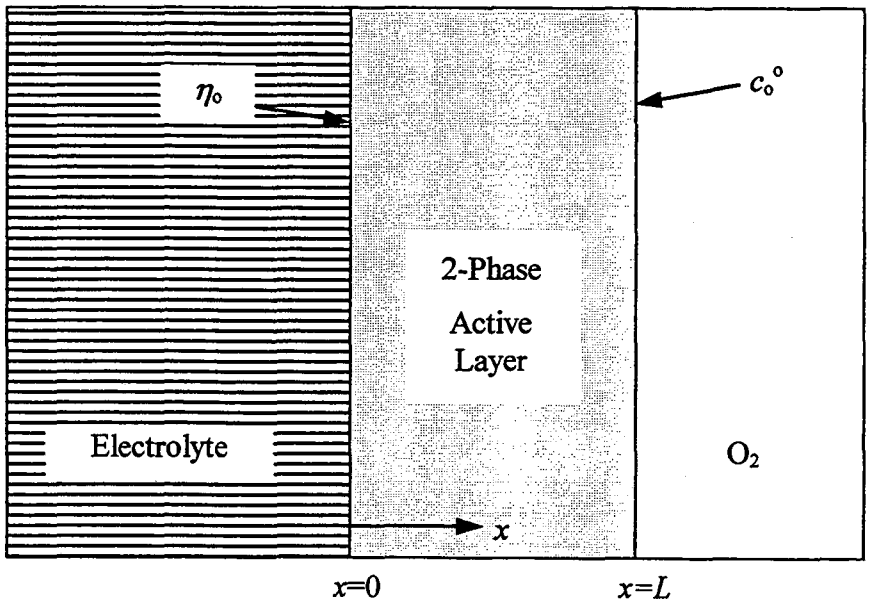

Figure 4-2. Schematic Diagram of Polymer-Electrolyte Model.

$$i_2 = -\kappa_e \frac{\partial \Phi_2}{\partial x} = \kappa_e \frac{\partial \eta}{\partial x} \tag{4-19}$$

where $\kappa_e = \kappa(\varepsilon/\tau)$ is the effective conductivity of the electrolyte in the catalyst layer, and ohmic losses in the solid matrix are again considered negligible. A material balance on the oxygen yields:

$$\frac{\partial i_2}{\partial x} = n\mathrm{F}\, R_{ORR} = -n\mathrm{F}\, \mathscr{D}_o \frac{\partial^2 c_o}{\partial^2 x} \tag{4-20}$$

where the expression for R_{ORR} is given by Eqn. 4-3.

The derivative of Eqn. 4-19 may be combined with the first part of Eqn. 4-20 and rearranged to reduce the model to two dimensionless equations:

$$\frac{\partial^2 c_o^*}{\partial x^{*2}} = c_o^* \exp\left(\psi_p\right) \tag{4-21}$$

$$\frac{\partial^2 \psi_p}{\partial x^{*2}} = \phi\, c_o^* \exp\left(\psi_p\right) \tag{4-22}$$

where: $c_o^* = c_o / c_o^o$, $x^* = x / L$, $\psi_p = \eta^* + \ln(a_a\, k L^2 / \mathscr{D}_o)$, $\eta^* = -2.3\ \eta / b$, and

$$\phi = \frac{2.3 n\mathrm{F}\, \mathscr{D}_o\, c_o^o}{b\, \kappa_e} = \frac{2.3 n\mathrm{F}\, D_o\, c_o^o}{b\, \kappa} \tag{4-23}$$

with the boundary conditions:

$$\begin{aligned} &(i) \quad \text{at } x^* = 0, \quad \frac{\partial c_o^*}{\partial x^*} = 0, \quad \text{and} \quad \psi_p = \psi_p^o \\ &(ii) \quad \text{at } x^* = 1, \quad c_o^* = 1, \quad \text{and} \quad \frac{\partial \psi_p}{\partial x^*} = 0 \end{aligned} \tag{4-24}$$

Where ψ_p° is determined by a given reference electrode located just outside the electrode-electrolyte interface (at $x = 0$), and therefore, η_o is directly related to the experimentally measured half-cell potential.

Analogous to P, ϕ is not only proportional to the oxygen concentration in the polymer electrolyte but is also a ratio of the permeability of oxygen in the active layer and the ionic conductivity of this layer. The value of this parameter is quite sensitive to the amount of water present in the polymer electrolyte since, as stated above, the transport properties are a strong function of water content. For example, $\mathscr{D}_O c_o^\circ$ was estimated to be $\sim 10^{-12}$ mol/cm·s·atm at 80° C by Bernardi and Verbrugge for their PEFC model [61] from data taken on a Nafion® membrane in contact with a 0.5 M K_2SO_4 solution [62]; whereas LANL researchers have estimated $\mathscr{D}_O c_o^\circ$ to be $\sim 10^{-9}$ mol/cm·s·atm, at the same temperature, both from modeling fits [63] and from AC impedance measurements on actual PEFC GDEs [64]. Springer *et al.* [63] noted this large discrepancy and suggested "oxygen diffusion along grain boundaries as a possible explanation." However, another important cause for this larger than expected discrepancy can be attributed to the fact that the amount of water present in a PFSA membrane is much lower when the membrane is exposed to pure water vapor than when it is immersed in pure water [65], this phenomenon being known as Schroeder's paradox [66]. In any case, the latter value is probably a better estimate for this product in a PEFC electrode, unless the electrode is flooded with liquid water.

The ionic conductivity varies almost linearly with water content [59], and $\kappa \sim 10^{-3}$ to 10^{-1} S/cm for a PFSA under realistic PEFC operating conditions [59, 67]. The Tafel

slope b, in the potential regime where the ORR occurs on oxide-free platinum, is on the order of 100 mV [67]. Based on these estimates, a range of 10^{-4} to 10^{2} should encompass the realistic values of ϕ with $p_o \sim 0.1$ to 1 atm.

Eqns. 4-22 and 4-23 were also solved numerically with BAND, and the computer program is given in Appendix A.

4.2 Results and Discussion

4.2.1 Liquid-Electrolyte Model

Fig. 4-3 shows the numerical results of the liquid-electrolyte model for a PAFC cathode with three different values of the parameter P. Note that the results are shown as a Tafel plot with an ordinate showing increasing negative ψ, which is proportional to the potential of the cathode Φ_1; this plot therefore resembles the typical polarization curves presented for both full and half-cell data with increasing cell potential as the ordinate.

It was determined that there are four distinct regions which may arise on such a polarization curve:

Region (1), a kinetically controlled region, with the normal Tafel slope and first-order in oxygen partial pressure,

Region (2), controlled by kinetics and the diffusion of dissolved oxygen, showing a double Tafel slope and first-order in oxygen partial pressure,

Region (3), controlled by kinetics and ionic mass transport, showing a double Tafel slope and half-order in oxygen partial pressure,

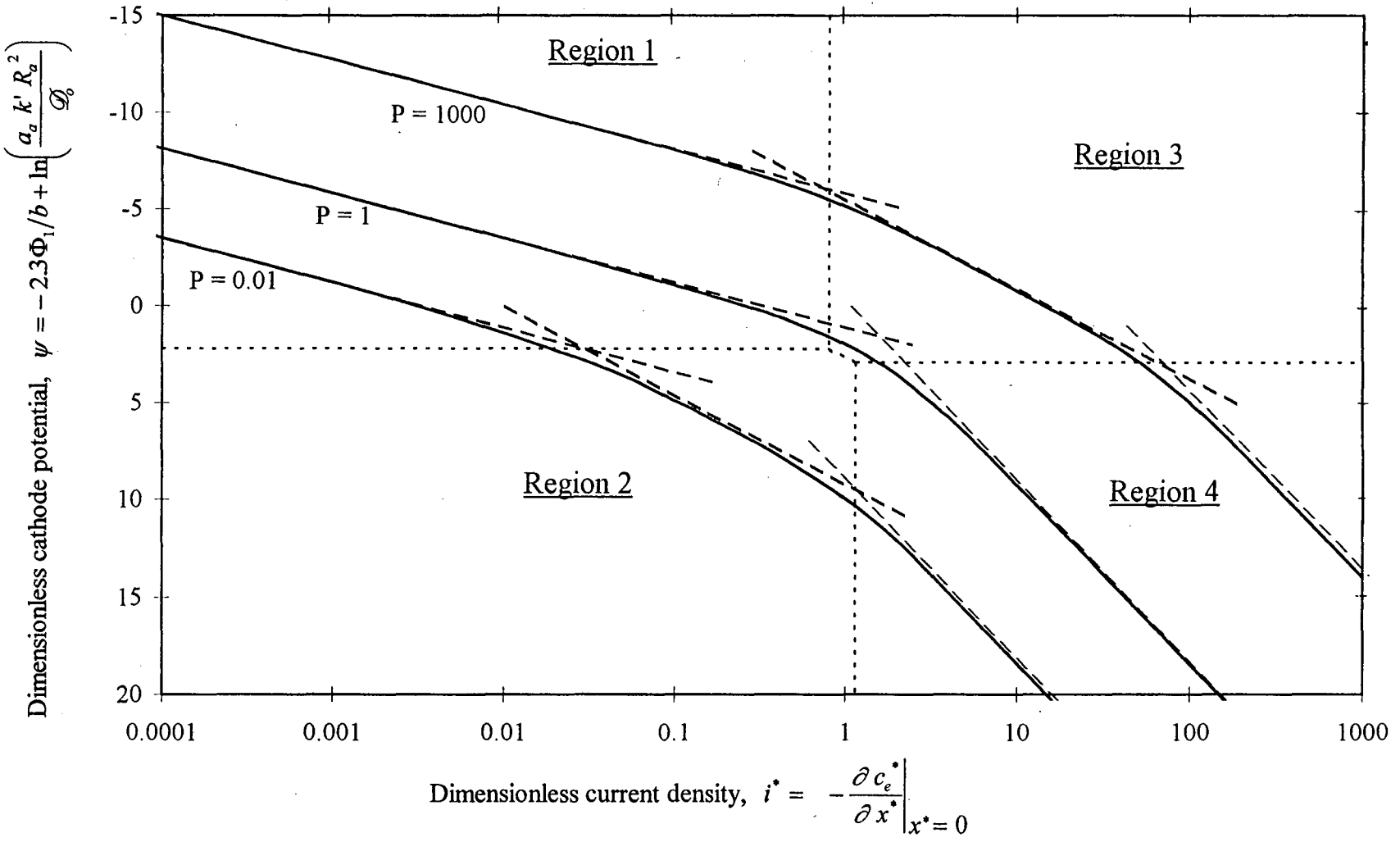

Figure 4-3. Tafel plot of liquid-electrolyte-model results for a PAFC cathode with $\theta = 3/4$.

Table 4-2. Asymptotic solutions and region boundaries of liquid-electrolyte model. Derivation of these equations are given in Appendix B.

Region 1 Normal Tafel slope First-order in c_o $i^* = -\left.\frac{\partial c_e^*}{\partial x^*}\right\|_{x^*=0} \approx \frac{P}{3} e^{\psi}$ $c_e^* \approx 1, \quad e^{\psi/2} << 1$	Region 1-3 Boundary A vertical line $i^* \approx \frac{2}{2\theta+1}$	**Region 3** Double Tafel slope Half-order in c_o $i^* \approx \left(\frac{2/3\,P}{2\theta+1}\right)^{1/2} e^{\psi/2}$ $c_e^* << 1, \quad e^{\psi/2} << 1$
Region 1-2 Boundary A horizontal line $e^{\psi/2} \approx 3$	Region 2-3 Boundary A double Tafel slope line $i^* \approx \sqrt{\frac{2/3}{2\theta+1}}\, e^{\psi/2}$	Region 3-4 Boundary A horizontal line $e^{\psi/2} \approx 3\left(\frac{2\theta+1}{\theta+1}\right)$
Region 2 Double Tafel slope First-order in c_o $i^* \approx P\, e^{\psi/2}$ $c_e^* \approx 1, \quad e^{\psi/2} >> 1$	Region 2-4 Boundary A vertical line $i^* \approx \frac{2}{\theta+1}$	**Region 4** Quadruple Tafel slope Half-order in c_o $i^* \approx \left(\frac{2\,P}{\theta+1}\right)^{1/2} e^{\psi/4}$ $c_e^* << 1, \quad e^{\psi/2} >> 1$

Region (4), controlled by kinetics, the diffusion of dissolved oxygen, and ionic mass transport, showing a quadruple Tafel slope and half-order in oxygen partial pressure.

The approximate boundaries of these four regions are depicted in Fig. 4-3; these boundaries were derived from asymptotic solutions of Eqn. 4-16. These approximate analytic solutions are shown in Table 4-2, along with the region boundaries plotted in Fig. 4-3; the latter were derived by simply equating the appropriate asymptotic solutions. The approximations used for the values of c_e^* and $\exp(\psi/2)$ in each region are also shown in Table 4-2, and the complete derivation of these asymptotic solutions is given in Appendix

B. The fact that the Tafel slopes and the oxygen partial pressure dependence for the four regions are as stated above can be clearly seen in these asymptotic solutions. The asymptotic solutions are also shown in Fig. 4-3, as dashed lines, and are in good agreement with the numerical results within their respective regions.

The validity of the assumptions used to derive the asymptotic solutions may be checked by plotting the oxygen and electrolyte concentration profiles predicted by the complete model for a range of current densities. Fig. 4-4 shows oxygen concentration profiles in an agglomerate at the electrolyte-electrode interface for $P = 0.001$, and Fig. 4-5 shows electrolyte concentration profiles across the active layer for $P = 1000$. The electrolyte concentration profiles are similar for all values of P at a given current density, which is as expected since the current is proportional to $\partial c_e/\partial x$ at $x = 0$. Therefore, at the current densities shown in Fig. 4-4, ionic transport is not very significant for $P = 0.01$, and the electrode is controlled primarily by kinetics and oxygen mass transport. On the other hand, oxygen transport is not significant for $P = 1000$ with $i^* < 10$ (the average value of c_o^* is 0.951 at $i^* = 10$), and the electrode is controlled primarily by kinetics and ionic transport in this region.

There are three types of polarization curves according to the model, as shown in Fig. 4-3. When P is equal to the "transitional" value P_x:

$$P_x \approx \frac{2/3}{2\theta + 1} \tag{4-25}$$

then ionic and dissolved oxygen transport both become significant at approximately the same current density. This yields a curve which changes from a normal Tafel slope directly to a quadruple Tafel slope. When P is greater than the transitional value, then the

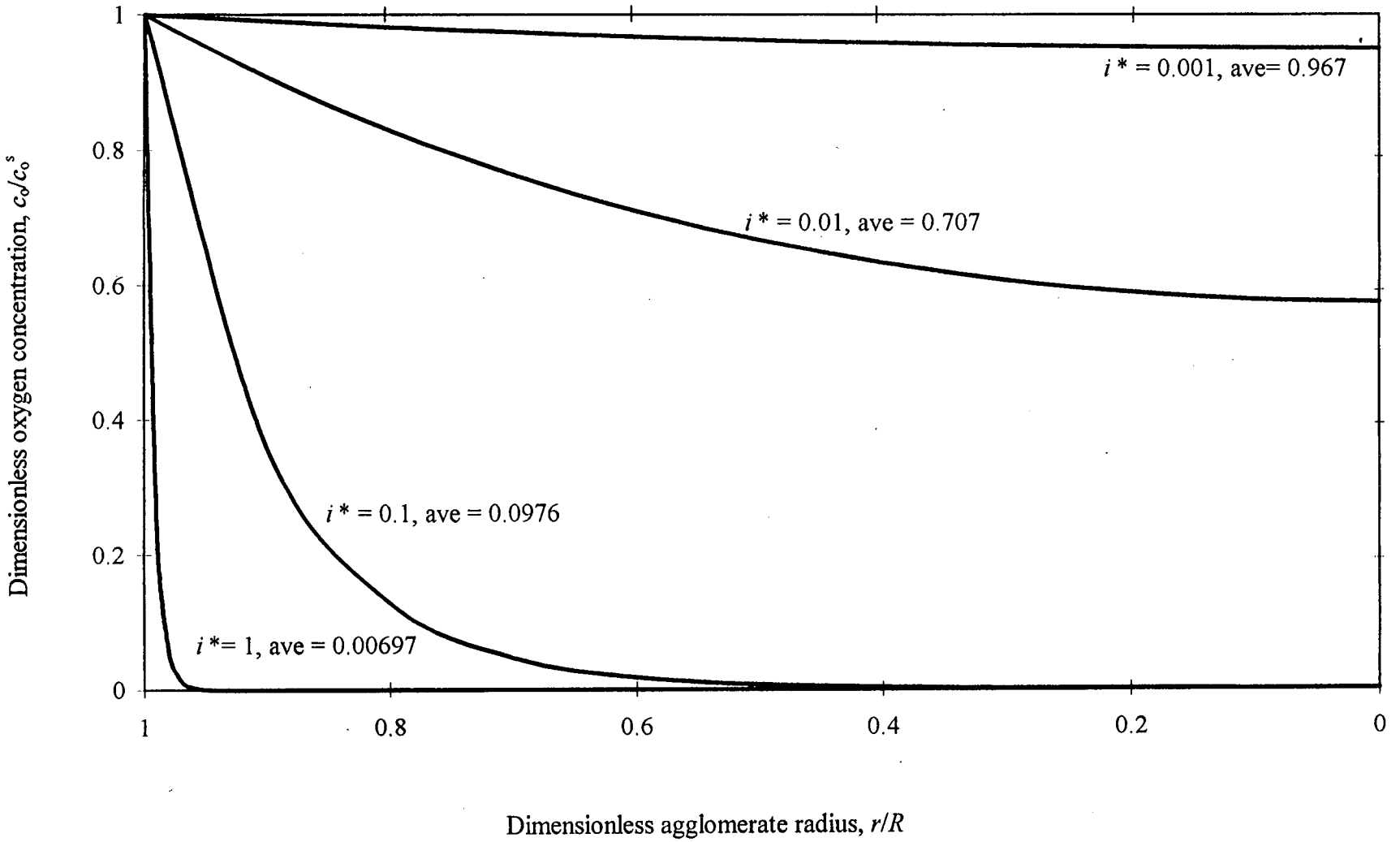

Figure 4-4. Oxygen concentration profiles in an agglomerate at $x = 0$ with $P = 0.001$.

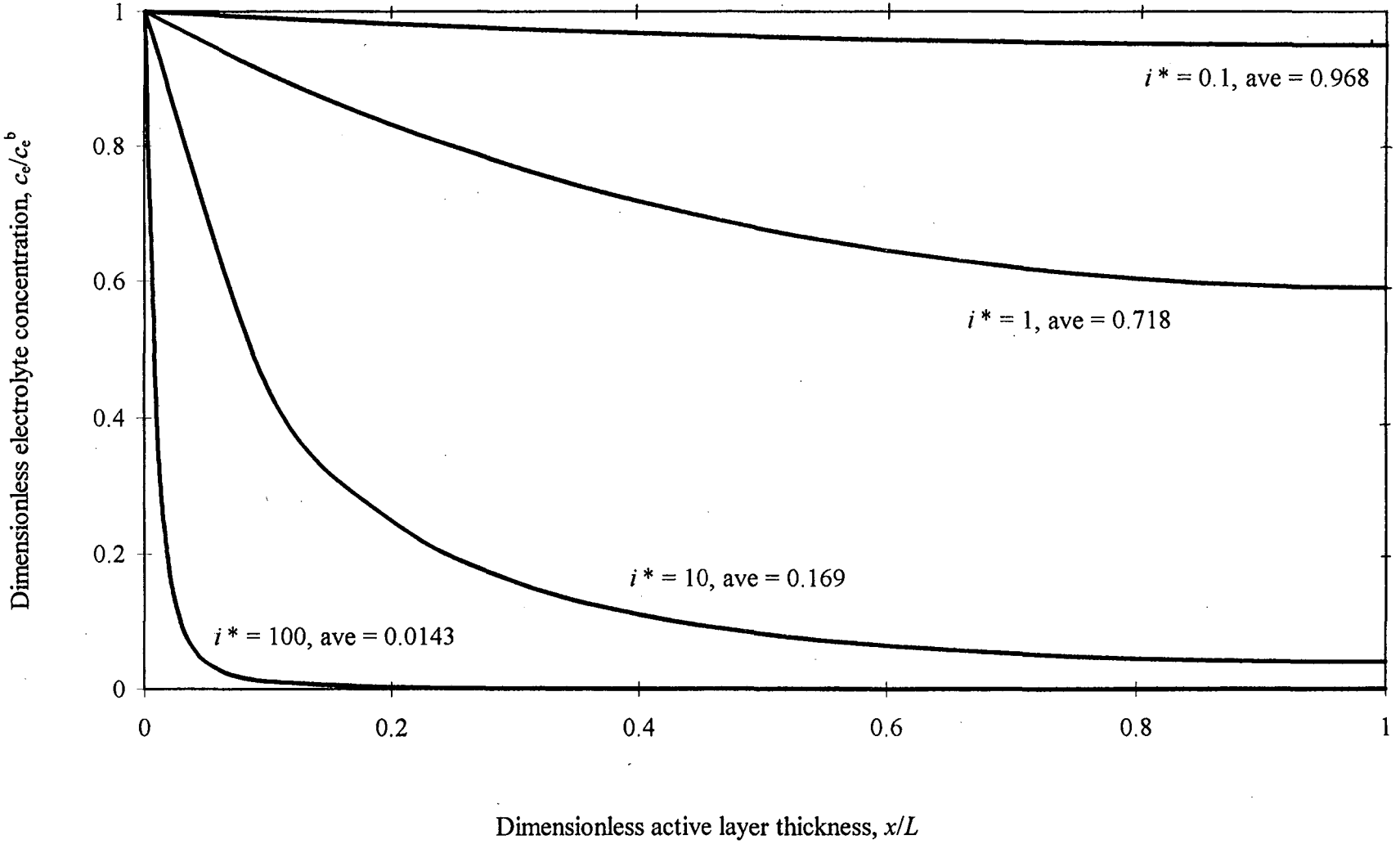

Figure 4-5. Electrolyte concentration profiles in active layer with $P = 1000$.

effect of ionic transport becomes significant at lower current densities than the effect of oxygen transport, causing a double-Tafel-slope region to appear, before the latter also becomes significant at even higher current densities resulting in a quadruple Tafel slope. This will be referred to as Region 1-3-4 behavior. With P values less than the transitional value, a Region 1-2-4 curve results, where dissolved oxygen-transport effects become significant first. Note that the relative length of the double Tafel slope region is proportional to the ratio of P/P_x.

By comparing the estimated values of P for AFC and PAFC cathodes with their respective transitional values (also shown in Table 4-1), it is readily apparent that a cathode with a KOH electrolyte will usually follow Region 1-2-4 behavior, unless a relatively thick catalyst layer is employed ($L > 1000\ R_a$). Therefore, one should normally expect this cathode to be first-order with respect to p_o, as predicted previously [25]; and the limiting current density due to oxygen mass-transport limitations is likely to be reached before ionic mass-transport effects become significant. On the other hand, it is reasonable to expect that PAFC cathodes may display any of the three types of polarization curves described above, depending on the operating conditions and the structure of these electrodes.

Table 4-1 also demonstrates that, for a given system, P is a strong function of the geometry of the GDE, in particular the ratio L/R_a. Changes in these dimensions will typically result in much larger variations of P for a given fuel-cell system than changes in the oxygen partial pressure and/or changes in the temperature and composition of the electrolyte.

Variations in the parameter θ will result in changing the potentials and current densities defining the boundaries between the regions, and this relationship is apparent in the asymptotic solutions given in Table 4-2. However, the value of this parameter, which includes the reaction order with respect to protons γ_+ (or hydroxyl ions, γ_-) and the value of the Tafel slope b, does not affect the general behavior stated at the beginning of this section. Even if the ORR were insensitive to *p*H, the model predicts that the double and quadruple Tafel slopes would arise due to mass-transport limitations. In the case of ionic-transport limitations, the change in Tafel slope results from the variation in the electrolyte potential Φ_2 due to the concentration variation (*i.e.*, a potential variation due to the diffusion potential). This will be discussed at length in Section 4.3.

One should note in Fig. 4-3 that the changes in Tafel slope due to ionic-transport limitations (*i.e.*, transition from Region 1 to 3 or from Region 2 to 4) occur at approximately the same current density for all P. This is not surprising, since the current is proportional to the electrolyte concentration gradient at the electrolyte-electrode interface. On the other hand, the transitions due to oxygen-transport limitations (*i.e.*, from Region 1 to 2 or from Region 3 to 4) occur at approximately the same dimensionless potential ψ for all P in Fig. 4-3. This is because the rate of consumption of oxygen is determined by the potential. However, it should be emphasized here that the dimensionless potential ψ also contains a ratio of the reaction rate to the rate of diffusion through an agglomerate (the square of the Thiele modulus for a nonelectrochemical porous-catalyst particle [68]). Therefore, for a given electrode these transitions will occur at approximately the same

cathode potential, but this value may change with changes in the GDE that affect a_a, k', $\mathscr{D}_o$, or R_a.

The asymptotic solutions and the region boundaries in Table 4-2 are expressed in terms of dimensionless potentials and current densities. However, one is interested in how changes in the physical variables will affect the actual current density. This is provided by the following proportionalities, which were derived from the approximate asymptotic solutions: In Region 1,

$$i \propto \; a_a \, k' \left(1-\varepsilon_l\right) L \, c_o^{\,s} \exp\left(-2.3\,\Phi_1/b\right) \tag{4-26}$$

in Region 2:

$$i \propto \; \left(a_a \, k' \, \mathscr{D}_o\right)^{1/2} \frac{\left(1-\varepsilon_l\right)}{R_a} \, c_o^{\,s} \exp\left(-2.3\,\Phi_1/2b\right) \tag{4-27}$$

in Region 3,

$$i \propto \; \left[a_a \, k' \, \mathscr{D}_e \left(1-\varepsilon_l\right) c_o^{\,s} \, c_e^{\,b}\right]^{1/2} \exp\left(-2.3\,\Phi_1/2b\right) \tag{4-28}$$

and in Region 4,

$$i \propto \; \left(a_a \, k' \, \mathscr{D}_o\right)^{1/4} \left[\mathscr{D}_e \frac{\left(1-\varepsilon_l\right)}{R_a} \, c_o^{\,s} \, c_e^{\,b}\right]^{1/2} \exp\left(-2.3\,\Phi_1/4b\right) \tag{4-29}$$

Note that these expressions are written in terms of the *p*H-independent rate constant k'; this is because the cathode potential Φ_1 should be measured relative to a given reference electrode located in the bulk electrolyte solution, ideally just outside the double layer at the electrode-electrolyte interface. (Although a concentration gradient may also form at this interface, this gradient will be less pronounced than the gradient within the active layer where diffusion is restricted by the pores and the reaction is consuming an ionic species.

This gradient effect should be negligible in concentrated fuel-cell electrolytes, and ideally this reference electrode should actually be located outside the cell via a capillary tube.)

The boundaries between the four regions may also be expressed in a similar manner. As stated above, the Region 1-3 and Region 2-4 transitions both occur at approximately the same current density i_x, which is proportional to:

$$i_x \propto \frac{\mathscr{D}_e c_e^{\,b}}{L} \tag{4-30}$$

whereas, the Region 1-2 and Region 3-4 transitions both occur at approximately the same potential $(\Phi_1)_x$ for a given cathode, which is proportional to:

$$(\Phi_1)_x \propto b \ln\left(\frac{\mathscr{D}_o}{a_a k' R_a^{\,2}}\right) \tag{4-31}$$

4.2.2 Polymer-Electrolyte Model

Fig. 4-6 shows the numerical results of the polymer-electrolyte model as a Tafel plot with three different values of the parameter ϕ. This model also predicts two distinct double Tafel slopes, one arising from control by kinetics and oxygen transport and the other due to control by kinetics and ionic transport. These results are not surprising, since the PEFC GDE was considered to have essentially the same structure as a flooded-porous electrode and the phenomenon of two distinct double Tafel slopes with these electrodes has been known for quite some time. For example, Austin [26] examined the importance of these two mass-transport effects on the basis of a ratio which is similar to ϕ. One can use the same asymptotic approach Austin employed to derive approximate solutions for the three regions depicted in Fig. 4-6; at low current densities (Regions 1 and 2), the

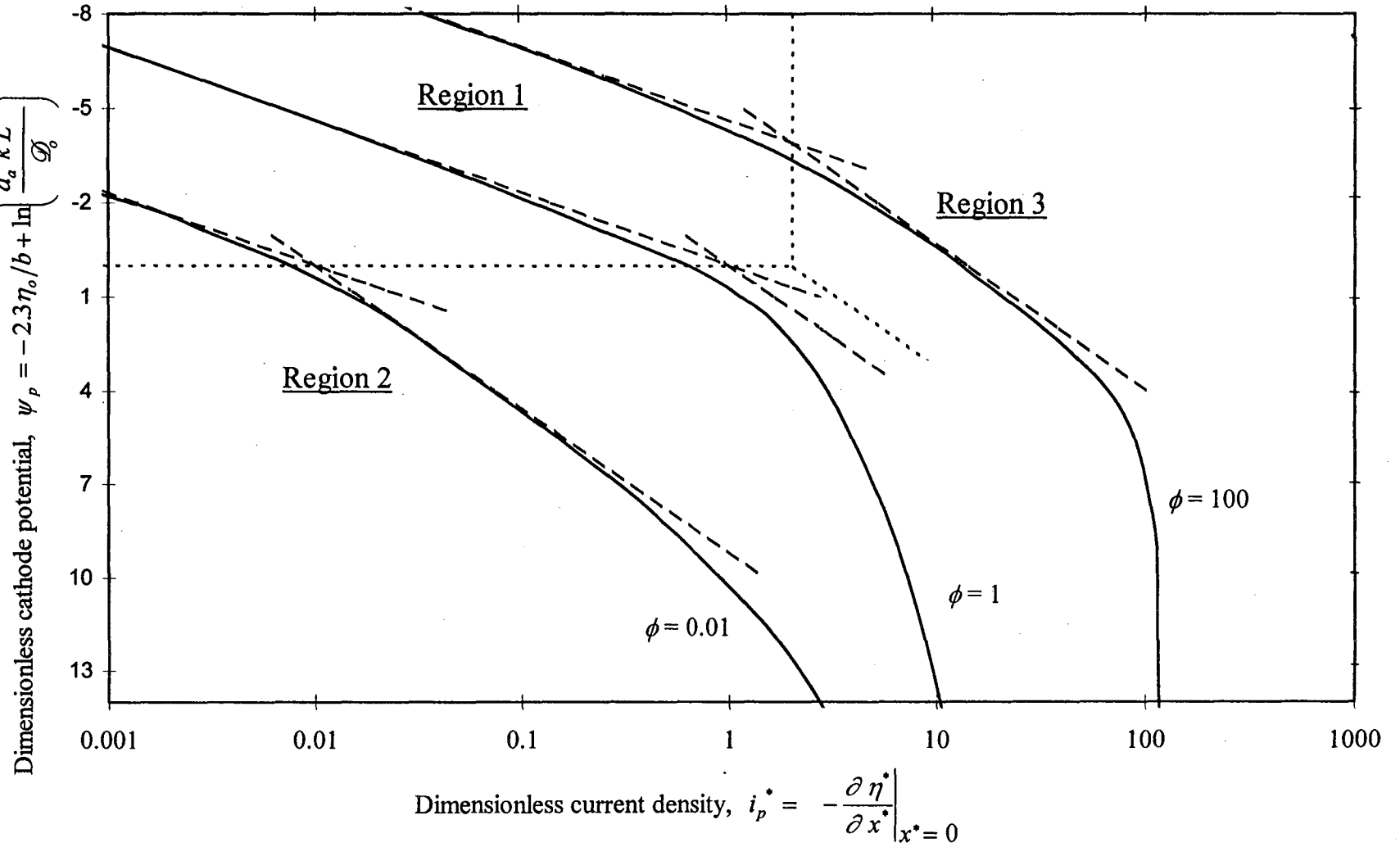

Figure 4-6. Tafel plot of polymer-electrolyte-model results for three values of the dimensionless parameter ϕ.

potential drop across the active layer is assumed to be negligible (*i.e.*, $\eta^* \approx \eta_o^*$ across L), and at higher current densities where oxygen-transport limitations are still negligible (*i.e.*, Region 3, where $c_o \approx c_o^o$ across L) the potential drop across the active layer is assumed to be quite large (*i.e.*, $\exp(\eta_o^* - \eta_L^*) >> 1$). This approximation yields the following:

In Region 1,

$$i \approx nFa_a k c_o^o L \exp(-2.3\eta_o/b) \tag{4-32}$$

in Region 2,

$$i \approx nF\sqrt{a_a k \mathscr{D}_o} c_o^o \exp(-2.3\eta_o/2b) \tag{4-33}$$

in Region 3,

$$i \approx \sqrt{2nFa_a k c_o^o \kappa_e b/2.3} \exp(-2.3\eta_o/2b) \tag{4-34}$$

These asymptotic solutions may also be expressed in dimensionless form: $i_p^* \approx \phi \exp(\psi_p)$ in Region 1, $i_p^* \approx \phi \exp(\psi_p/2)$ in Region 2, and $i_p^* \approx \sqrt{2\phi} \exp(\psi_p/2)$ in Region 3. These asymptotes, and the definition of i_p^*, are shown in Fig. 4-6.

Like the liquid-electrolyte model, this model predicts a first-order dependence on oxygen concentration when the GDE is controlled by kinetics or by kinetics and oxygen transport (Regions 1 and 2), whereas the dependence is half-order with respect to oxygen when the GDE is controlled by kinetics and ionic mass transport (Region 3). The main difference between the results of this model and the liquid-electrolyte model is the absence of a well-defined Region 4. When kinetics, oxygen mass transport, and ionic transport all become significant, the polarization curve does not display a simple multiple Tafel slope or a well-defined oxygen dependence, as before. In this case the performance decays rapidly, and this behavior will be fully explained in the next section.

The boundary between Regions 1 and 3 is $i_p^* \approx 2$, and therefore:

$$i_x \propto \frac{\kappa_e b}{L} \tag{4-35}$$

And the boundary between Regions 1 and 2 is $\psi_p \approx 1$, and therefore:

$$(\eta_o)_x \propto b \ln\left(\frac{\mathscr{D}_o}{a_a k' L^2}\right) \tag{4-36}$$

These two relations are analogous to Eqns. 4-30 and 4-31 from the previous model.

In this case, the transitional value of the parameter ϕ is $\phi_x = 2$. And the relative length of the double Tafel slope region is again proportional to the ratio of this parameter and the transitional value (*i.e.*, ϕ/ϕ_x); however, even before $\phi \cong \phi_x$ the double Tafel slope disappears, as shown in Fig. 4-6 for $\phi = 1$. From the rough estimate of the range of ϕ given in the previous section, it is apparent that three types of polarization curves may be realistically anticipated for a PEFC cathode, as was the case with a PAFC cathode. Once again, high-pressure operation will favor ionic-transport effects becoming significant prior to oxygen transport; and a relatively dry cathode is more likely to be ionically limited, whereas oxygen-transport effects will most likely dominate the performance of a flooded cathode.

4.3 Physical Explanation of Results

One should develop an intuitive feeling for how and why the oxygen cathode behaves in the manner predicted above in order to utilize fully the results of the mathematical analysis. The first-order oxygen dependence in the case of control by kinetics and oxygen transport is easy to understand, since both of these processes are also-first order;

however the half-order dependence that results from ionic transport is not so intuitive. In order to understand this half-order oxygen dependence, one needs first to understand the origin of the double Tafel slope. Although the occurrence of a double Tafel slope is well accepted, and has been derived mathematically in a variety of ways, the physical processes that account for this phenomenon have not generally been elucidated in the literature.

We shall therefore start with a physical explanation for the double Tafel slope that results as a consequence of control by kinetics and oxygen mass transport (*i.e.*, Region 2 in these models). At low current densities, where mass transport is not significant, Fig. 4-4 shows that increasing the current by an order-of-magnitude does not result in a large change in the oxygen profile. However, at higher current densities an order-of-magnitude change does result in a large change in the profiles, and since the ORR kinetics are first-order in oxygen this change will cause the total current produced in the agglomerate I_a to be significantly less than the current that would result if all of the catalyst surfaces inside the agglomerate were exposed to an oxygen concentration equal to that at its surface. Hence, the rate is controlled by oxygen transport, in addition to kinetics, at these high current densities where the oxygen profiles are very nonuniform.

We can be more quantitative about the effect of mass transport by first noting two simple proportionalities: *i*) the areas under the oxygen profile curves in Fig. 4-4 are proportional to the current produced in the agglomerate I_a, and *ii*) I_a is also proportional to the slope of the oxygen profile curve at $r/R_a = 1$. (The first relation holds because I_a is proportional to the integral of the local reaction rate R_{ORR} throughout the agglomerate, which is in turn proportional to the local value of c_o. The second relation comes from the fact that, at steady state, I_a is proportional to the total flux of oxygen into an agglomerate,

which is proportional to the oxygen gradient at the surface of the agglomerate). Next, we note a relationship that exists only at high current densities, when the slope at $r^* = 1$ of these profiles becomes greater than c_o^s/R, (*i.e.*, > 1) in Fig. 4-4, the area under the curve decreases by roughly the same amount that the initial slope increases as the current is increased. This relationship is demonstrated in Fig. 4-4 by the average c_o value given for each curve, which is proportional to the area under the given curve. This relationship may also be readily deduced graphically by using triangles to approximate the oxygen profiles in the high-current-density region, and noting that changing the slope is equivalent to changing the angle at the apex of the triangle, which results in a proportional change to the base of the triangle, and thereby the area of the triangle.

One can now readily understand the square-root dependence that results by performing an example using this simple "triangle" approximation for the region controlled by oxygen mass transport. Let us assume that we increase the local reaction rate to four times its previous value, $R_{ORR}' = 4\ R_{ORR}$, by holding the electrode potential constant and increasing the temperature such that the reaction rate constant increases four-fold. At low over-potentials, where mass transport is not significant, this would result in a fourfold increase in the current density, *i.e.*, $I_a' = 4\ I_a$. However, at a high overpotentials, where mass transport is dominant, I_a cannot increase by four times since this would cause the average oxygen concentration, or area of the oxygen profile "triangle," to decrease by four times as well, and I_a' must also be proportional to four times this new area. These two competing effects, the increase in the kinetic driving force which causes a corresponding decrease in the average oxygen concentration, will reach equilibrium at a condition wherein the actual rate increase is just equal to the resulting decrease in the average

oxygen concentration. In other words, the rate will increase by the square root of the increase in the kinetic driving force. In this example, $I_a' = 2\, I_a$, which is proportional to four times the area of the new "triangle," which is now one-half its previous value.

One should note that the preceding argument holds for all the terms in the ORR kinetic rate expression, Eqn. 4-3, except for c_o.. When c_o is changed, this also changes the height of the "triangle," and thereby the area by a proportional amount, so the reaction is still first order in oxygen in this region (see Eqn. 4-26). It should also be pointed out that the above analysis is analogous to that for the familiar chemical-engineering problem of a porous-catalyst pellet with a first-order reaction controlled by mass-transport limitations of the reactant, which is why the Thiele modulus is the square root of $(k\, a/D)$ for this system [68]. This explanation also holds for the polymer-electrolyte model, where the entire active layer may be considered to be a single pellet or agglomerate.

The double Tafel slope in Region 3 is also a result of limited mass transport; however, it is not necessarily the result of a concentration gradient. In this case the origin of the double Tafel slope is ohmic in nature, and is analogous to the double Tafel slope illustrated by Newman and Tobias [69] for a porous battery electrode with $\kappa << \sigma$, where σ is the conductivity of the solid matrix. At sufficiently high current densities, the flux of ions participating in the cathodic reaction (*i.e.*, protons or H_3O^+ in an acid electrolyte) creates a significant gradient of potential in the electrolyte phase across the thickness of the active layer. In the case of a liquid electrolyte, this potential gradient is proportional to the log of the electrolyte concentration gradient, as shown by Eqn. 4-13. However, even in an electrode employing a polymer electrolyte, where the concentration of ions is

necessarily uniform, a relatively large potential gradient will develop at high current densities. The ions are driven solely by migration in this case, and this potential gradient is necessary in order to maintain the flux of ions required to maintain the rate of the reaction.

Although the situation is different from the previous case, we may once again use a graphical explanation in order to develop a physical understanding of the origins of this double Tafel slope. In this case, we examine the electrolyte concentration profiles across the thickness of the active layer L as shown in Fig. 4-5 for $P = 1000$, where the effects of oxygen mass transport are negligible. Since the potential gradient is proportional to the log of the electrolyte concentration gradient and the local reaction rate is proportional to the exponential of the local overpotential, the situation is analogous to the previous case where at high current densities the reduced value of a local variable (in this case the overpotential) causes the rate of the reaction throughout the depth of the electrode to be substantially less than the "surface rate." Once again, we may invoke the "triangle" approximation to gauge how the area under the curve varies in the very nonuniform region. Here the bases of the "triangles" are analogous to the concept of the "penetration depth" discussed by Winsel [70]. And, at high current levels, the penetration depth becomes inversely proportional to the total current, as shown by Newman and Tiedemann [22].

In the case where the ORR kinetics are first-order with respect to the electrolyte concentration, it may be tempting to think of this latter case as being completely analogous to the case controlled by the depletion of oxygen in the active layer. However, this is view incorrect, because irrespective of the electrolyte reaction order, a potential gradient will be formed which is the cause of the double Tafel slope in this case. This

reaction order does affect where the Tafel slope transition will occur (via θ in the liquid-electrolyte model), but even if the reaction is zero-order with respect to the electrolyte concentration (*e.g.*, KOH electrolyte) or the electrolyte concentration is essentially uniform (*e.g.*, a polymer electrolyte) an ohmic drop develops at sufficiently high current densities. One should also note that in this case, any change that would cause the kinetic rate of the ORR to increase, including an increase in the oxygen concentration or the electrolyte concentration, will result in half-order behavior, as shown by Eqns. 4-28 and 4-34 for Region 3.

One may now also understand the difference in the behavior predicted for the two models when both oxygen and ionic transport are significant. In the flooded-agglomerate model for liquid electrolytes these two types of mass transport simultaneously control the rate over two distinct length scales. Ionic transport determines the distance to which the reaction penetrates the active layer, and oxygen transport determines the distance to which the reaction penetrates the agglomerates. On the other hand, in the polymer-electrolyte model the two types of mass transport control the rate over a single length scale, the thickness of the active layer, and they propagate in opposite directions. The region most depleted of oxygen lies where the local overpotential is the highest and *vice versa*, and therefore, when both effects become significant, the total reaction rate rapidly drops as shown in Fig. 4-6.

4.4 Conclusions

The results of these models reinforce an important point that has been emphasized in previous models (both for flooded-porous electrodes and GDE's) – both the thickness of the active layer and the size of the agglomerates should be kept as small as possible to minimize the adverse effects of mass transport at high current densities. Only part of the electrocatalyst is effectively utilized when either the neutral reactant or the ions participating in the reaction cannot fully penetrate all parts of the electrode. For this reason, with sluggish reactions (such as the ORR or the direct anodic oxidation of alcohols or hydrocarbons at low temperatures) which require relatively high catalyst loadings to achieve relatively high current densities, it may be better to use an unsupported electrocatalyst rather than supported electrocatalyst. This conclusion is reached because, despite the lower specific surface area of the unsupported catalyst, the higher utilization resulting from their more compact structure may more than offset this difference at high current densities. (This trade-off must also be weighed against the greater propensity for unsupported electrocatalyst to sinter with age [71].)

One would optimally prefer that a fuel-cell cathode follow Region 1 behavior to as high a current density as possible. This will occur when either $P \geq P_x$ or $\phi \geq \phi_x$, since this will yield the maximum current density i_x for the transition to a double-Tafel-slope region. Note that an attempt to increase i_x results in a decrease in P or ϕ (see Eqns. 4-30 and 4-35), and therefore the maximum current density showing Region 1 behavior will be achieved with $P = P_x$ or $\phi = \phi_x$. If one wishes to operate at higher current densities than this value, then one should strive to operate in Region 3 (*i.e.*, with $P > P_x$ or $\phi > \phi_x$) since

this will yield higher currents at the same potential for a given cathode. However, in this region, the performance increases only with the square root of the operating pressure, and pressurization of the system is not nearly as effective as in Region 2.

The above conclusions should be qualified by the fact that practical fuel-cell cathodes may not be well described by these two rather simple models. Two of the model assumptions are especially tenuous for practical fuel-cell cathodes. The first is neglecting gas-phase mass transport; which may be a good assumption for a cathode operating on pure oxygen (although even in this case the mole fraction of O_2 is less than unity due to the presence of water vapor), but when the oxidant feed is air, gas-phase mass transport will usually be an important factor, especially at high current densities. Gas-phase mass-transport limitations may occur both within the catalyst layer itself and in the backing layer and/or the manifold of the cathode; thus, even in the polymer-electrolyte model, where such effects in the catalyst layer are implicitly taken into account, this may be poor assumption. The second important assumption is that the transport properties are constant. This may be an especially poor approximation for PEFC cathodes since the physical properties of the polymer electrolyte are very sensitive to the water content, which will vary with current density. This factor may be important for cathodes with liquid electrolytes as well, not only because of water effects (such as electrode flooding) but other factors as well, such as temperature gradients.

In regards to gas-phase mass transport in the catalyst layer of the liquid-electrolyte model, it should be noted that the polymer-electrolyte model effectively treats the limiting case wherein the transport of oxygen is dominated by gas-phase limitations. This may apply in the case of a liquid-electrolyte cathode where the porous-catalyst particles are

very small and the cathode operates on a feed with a low mole-fraction of oxygen. In this case, it is clear from the results of the latter model that two distinct double Tafel slopes still exist, one with a first-order dependence on p_o and one with a half-order dependence. No such simple conclusions may be made, however, regarding a flooded-agglomerate-type cathode when both gas-phase and liquid-phase transport of oxygen are significant.

Although more sophisticated models which include these important factors would certainly be of value, it is beyond the scope of the present work, and it is also doubtful that such simple results (double and quadruple Tafel slopes, reaction orders of one and one-half) will be predicted by such models. The real value of the present work is not to predict the full results of practical fuel-cell cathodes, but instead to illustrate these important limiting cases, which are important in developing an understanding of the much more complex behavior of complete fuel-cell systems. Additionally, these results may be used as a simple diagnostic tool to aid fuel-cell researchers in the optimization of cathodes. Such diagnosis can be carried out by testing the cathodes under conditions which favor the assumptions made above, and this process is the subject of the next chapter.

Chapter 5. Application of Modeling Results

"We must ask ourselves, what will we have learned from this work other than to show how smart we are?" — Charles W. Tobias

5.1 Diagnostic Tool for the Analysis of Fuel-Cell Cathode Performance

One may use the results presented in the previous chapter as a simple diagnostic tool to determine what mass-transport processes control a fuel-cell cathode at high current densities. This diagnosis may be performed by recording the polarization curves on a given cathode at different pressures of oxygen and plotting these data on a Tafel plot. Then by comparing the ratio of currents for two or more sets of data at a potential for which a double Tafel slope may appear, one may determine whether the behavior is first-order or half-order in oxygen concentration. This information may be very useful for the optimization of a GDE for a particular application. For example, one may seek to vary the value of P or ϕ (by changing the structure of the cathode, and/or the composition of the electrolyte, and/or the operating temperature or pressure) to obtain a desired behavior at a given current density.

Additionally, for a cathode employing a liquid electrolyte, it may be possible to estimate the value of the parameter P used in the liquid-electrolyte model directly from the data if the cathode polarization curves display both double and quadruple Tafel slopes. In this manner one readily obtains a quantitative measure of the relative importance of the two mass-transport effects considered in this model, which is useful for estimating how much the cathode parameters must be altered to obtain the desired performance. This

method is schematically illustrated in Fig. 5-1. All that is required is the two potentials at which the Tafel-slope transitions occur. Let $V_{1\text{-}2}$ represent the potential where the single and double Tafel slopes intersect, and $V_{2\text{-}4}$ represent the potential of intersection of the double and quadruple Tafel slopes. Then for Region 1-2-4 curves (first-order in p_o):

$$\frac{P}{P_x} \approx \frac{2\theta+1}{(\theta+1)\,10^{\beta}} \tag{5-1}$$

where $\beta = (V_{2\text{-}4} - V_{1\text{-}2})/b$. And, for Region 1-3-4 curves (half-order in p_o):

$$\frac{P}{P_x} \approx \frac{(\theta+1)^2\,10^{\beta}}{(2\theta+1)^2} \tag{5-2}$$

When attempting to use the model results as a diagnostic tool, one should keep in mind several important considerations. First, and foremost, are the two important model assumptions that were emphasized in Section 4-4. One must minimize both gas-phase

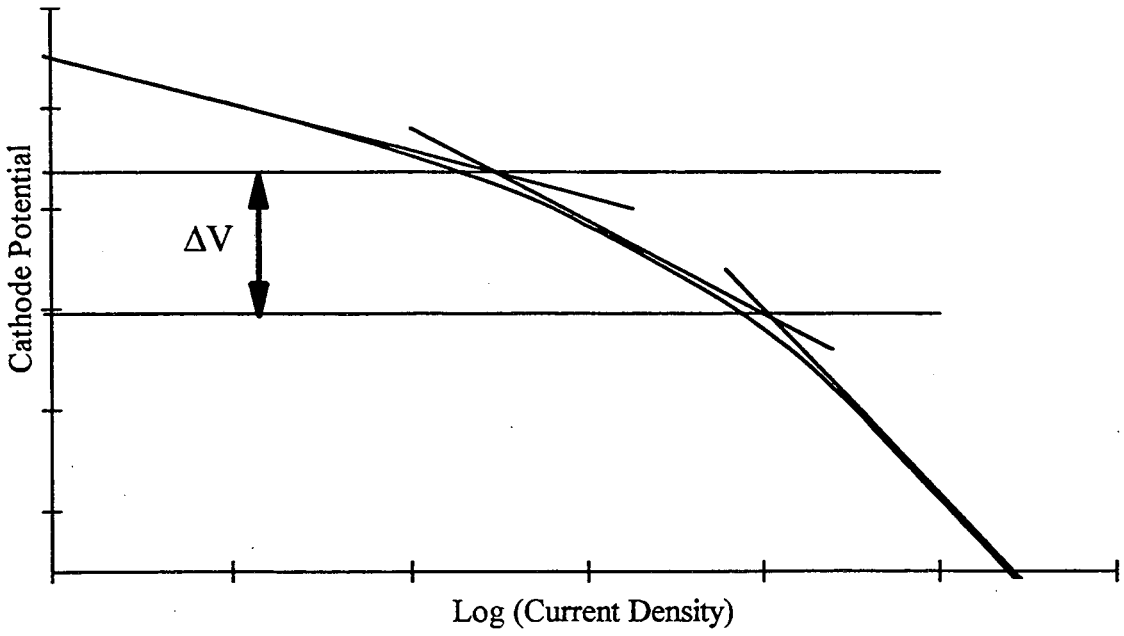

Figure 5-1. Illustration of graphical method for estimation of P directly from data.

mass-transport effects and variations in water content in the cathodes being tested in order to produce results that may be interpreted with the models presented here.

To obtain the best results, the polarization data should be taken at a very low oxygen utilization to minimize variations of p_o in the flow field or manifold. However, since the pressure drop increases as the square of the flow rate, the lowest flow rate which produces results that are relatively insensitive to further rate increases should be considered as optimal.

Minimizing the effects of gas-phase diffusion in the backing layer and the active layer is more challenging since, unlike the flow field, convection is not an important factor in these regions. Gas-phase transport in the active layer is implicitly accounted for by the polymer-electrolyte model; therefore, this effect is most important only when applying the results of the liquid-electrolyte model. Unfortunately, minimizing gas-phase transport in the active layer is inherently complicated in these GDE's, since increasing the hydrophobic porosity (*i.e.*, increasing the PTFE content) will also invariably result in a thicker active layer, all other factors being equal.

Employing cathode feeds with a high mole fraction of oxygen will help to minimize diffusive effects in the gas phase. One should keep in mind however, that even with a feed of pure oxygen, gas-phase diffusion may still play a significant role at high reaction rates since the partial pressure of water in the cathode is significant in any aqueous-electrolyte fuel cell operating at elevated temperatures.

One may determine the actual significance of gas-phase diffusion by comparing data recorded at different total pressures and the same oxygen partial pressure. For a given

p_o, gas-phase mass transport is more likely to be significant at higher total operating pressures, since (at the pressures of interest here) the diffusivities of gases generally vary inversely with pressure. However, if gas-phase diffusion is truly negligible, then all data taken at the same p_o should be essentially identical. At the other extreme, if the ratio of currents at a given potential are equal to the inverse ratio of the total pressures, then the cathode performance is dominated by gas-phase transport at that potential.

Although neglecting gas-phase mass transport may at first appear to be a severe limitation of this model, it should be noted that an efficient GDE must necessarily be designed such that these losses are minimized as much as possible. The design of a GDE is a classic optimization problem which may be conducted by using the method outlined in the previous paragraph to minimize gas-phase losses as the first step of each iteration. Of course, before beginning this optimization process, one needs to have an estimate of what the requirements are for the application in mind. The optimization of a GDE is also part of a larger optimization process which includes such factors as the utilization of reactants, operating temperature and pressure, and the costs associated with these variables. (Newman [72] has provided a simple method for conducting a cost analysis for the anode utilization and cell potential of a hydrogen fuel cell.) One should recognize that the data taken for this analysis may be collected at oxygen utilizations and partial pressures quite different from what is ultimately determined to be practical.

One should also attempt to minimize the effects of varying water content in the cathode when applying the results of this model, especially with a PEFC. The best PEFC performance will be obtained when the polymer electrolyte is fully hydrated without the

formation of large amounts of liquid water within the GDE's. Therefore one may strive to maintain this optimum, and relatively constant, hydration level by varying the humidification conditions of the feed streams and recording the data at the best conditions. Once again, this procedure may not yield realistic results for a practical PEFC, but it is a good strategy for using the diagnostic tool presented here, and it yields some additional interesting information – namely, identification of the best humidification conditions at a given current density.

One may be tempted to apply this diagnostic tool to *iR*-free data for a complete fuel cell operating on pure hydrogen, since the losses in the cathode dominate this system. (An additional linear term might be subtracted from such data to account for the anode polarization losses.) However, this approach should be discouraged, since this tool requires that data be collected at relatively high current densities, where the hydrogen electrode may no longer strictly follow linear kinetics, and mass-transport effects are likely to be significant in the anode as well. A reference electrode should be employed to measure the half-cell potentials.

It should also be re-emphasized that the ORR on Pt may exhibit a change in Tafel slope due solely to kinetic effects at potentials near the open-circuit value, greater than approximately 0.8 V *vs.* RHE [44]. This phenomenon is attributed to the change in oxide concentration on the Pt surface in this potential range [57], and may in fact cause the Tafel slope to double as well. Therefore, this model should be used with caution to interpret results in this complex region where one is measuring mixed potentials due to both the reaction and the changing oxidation state of the electrocatalyst. One should normally

determine a value for the "normal" Tafel slope at a potential less than approximately 0.8 V *vs.* RHE; hence the Tafel slope referred to herein may be considered the "apparent" Tafel slope, as was pointed out in the previous chapter. Oxides will also certainly form on other suitable electrocatalysts at high potentials, and one should be aware of the range of potentials for which the situation will be complicated by the resulting mixed potentials.

Finally, there are other factors not accounted for by the models which may affect the experimental measurements (*e.g.*, temperature gradients in the cell), especially at high current densities. One must apply the results cautiously and not force the tool to fit data that may be strongly influenced by factors not accounted for in the models.

5.2 Comparison of Model Results with Published Experimental Results

In order to test the validity of the models and to demonstrate the use of the results as a diagnostic tool, some comparisons of the model results with experimental data found in the literature will be presented in this section. Since the double-Tafel-slope behavior which results from oxygen-transport limitations is well accepted and has been confirmed experimentally [73], this section will focus on systems which appear to be controlled by kinetics and ionic transport.

5.2.1 Phosphoric-Acid Fuel-Cell (PAFC) Cathodes

From the results of the model, one would expect PAFC cathodes operating at elevated pressures with relatively thick catalyst layers and very small agglomerates (*i.e.*, high values of P) to be the most likely candidates to exhibit ionic mass-transport limita-

tions. Maoka [74] at the Toshiba Corporation has reported some half-cell data on GDE's with small supported platinum particles and a relatively high PTFE content of 50 w/o; and one set of this data is reproduced in Fig. 5-2. In this paper, Maoka presents data for four different catalyst loadings, and he shows that with pure O_2 the current density is proportional to the catalyst loading at 0.8 V *vs.* RHE (in the normal Tafel slope range), whereas the current is proportional to the square root of platinum content in the catalyst layer at 0.7 V *vs.* RHE (in the double-Tafel-slope range).

Even though Maoka's experiments were run at atmospheric pressure, this electrode structure is well-suited for minimizing the effects of oxygen transport. Nevertheless, Maoka attributes the double-Tafel-slope behavior and the catalyst-loading square-root proportionality to oxygen-transport limitations which "support the flooded agglomerate model" of Giner and Hunter [25]. However, if one also examines the reaction order with respect to the partial pressure of oxygen, as shown in Fig. 5-3, it is apparent that the cathode behavior is half-order in the potential range over which the data demonstrate a double or quadruple Tafel slope. Therefore, according to the model presented here, the double Tafel slope is due to ionic-transport limitations, which also produces a square-root proportionality with respect to the catalyst loading (see Eqn. 4-28).

Further evidence for control by ionic transport in this cathode is present in Fig. 5-2. Note that the transition from a normal to a double Tafel slope occurs at approximately the same current density on the oxygen and air polarization curves. This behavior is as expected for a transition caused by ionic-transport limitations, whereas if the transitions were due to oxygen-transport limitations one would expect them to occur at approxi-

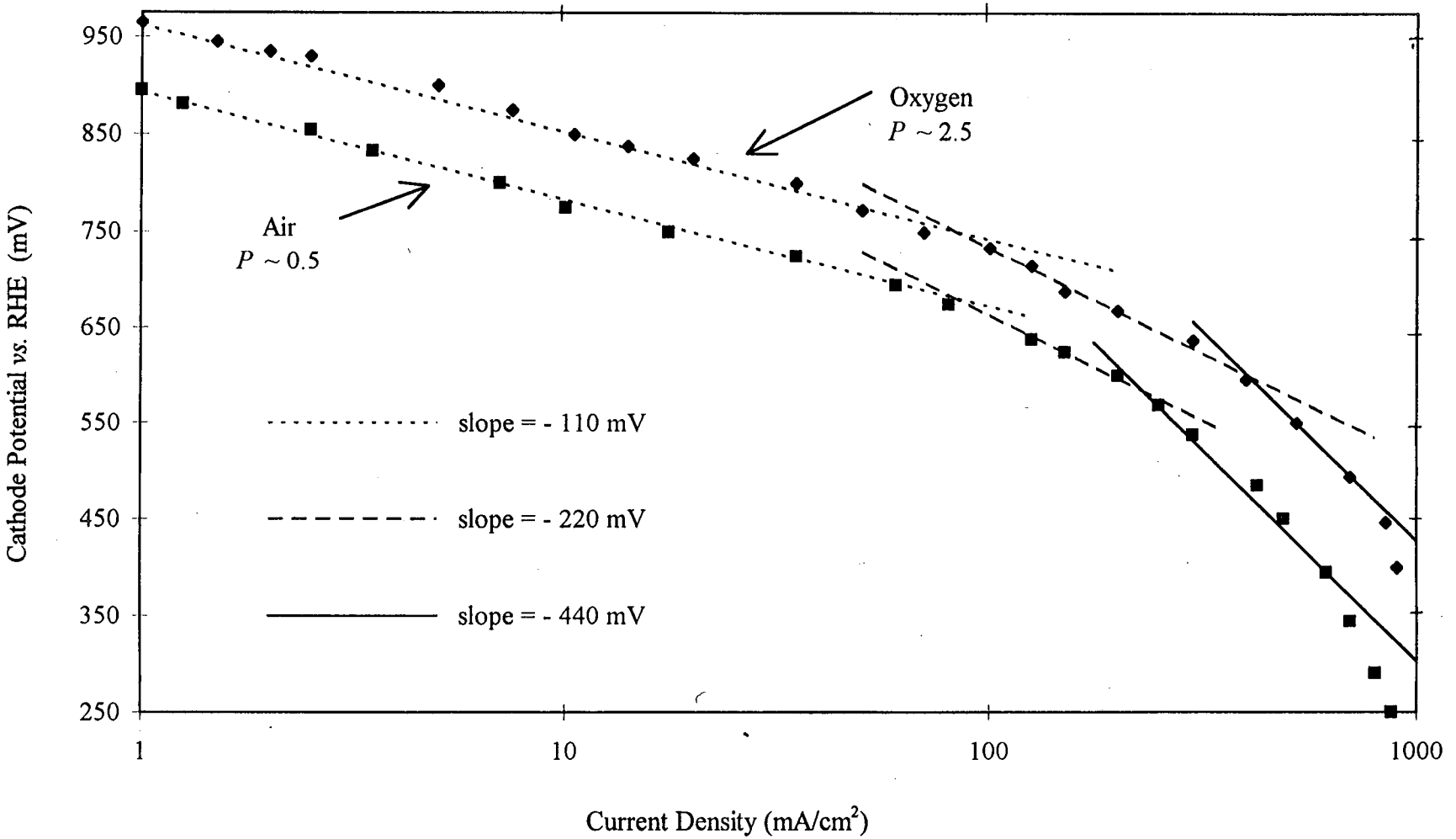

Figure 5-2. Tafel plot of cathode performance with 0.63 mg/cm^2 of Pt supported on Vulcan XC-72R and 50 w/o PTFE, taken at 190 °C and atmospheric pressure in 105 w/o H_3PO_4, as reported by Maoka [74].

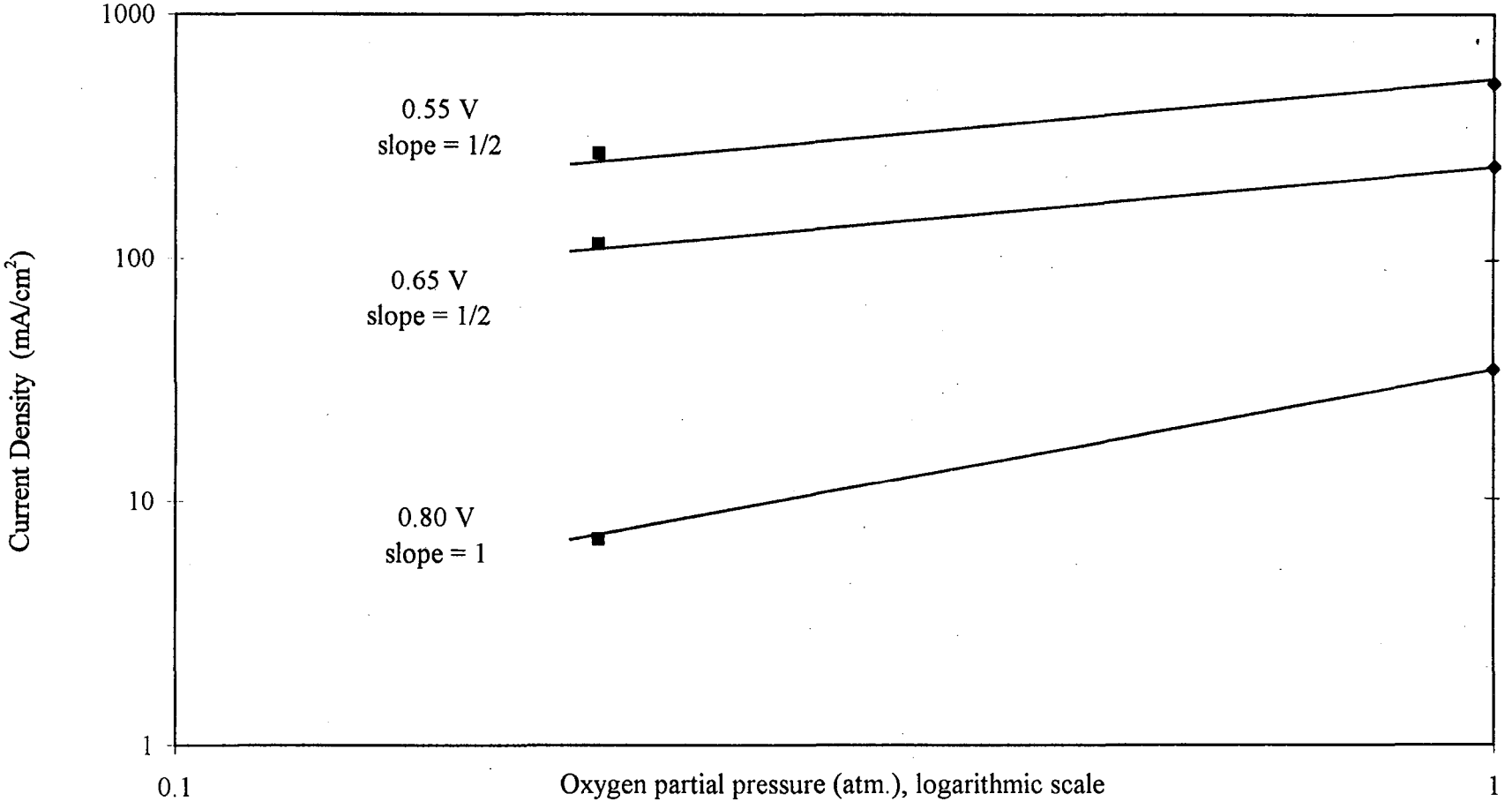

Figure 5-3. Oxygen dependence of data shown in Fig. 5-2 at three different cathode potentials.

mately the same potential, as is nearly the case for the double-to-quadruple Tafel-slope transitions.

Since the data in Fig. 5-2 also appear to display quadruple Tafel slopes, the method outlined in the previous section was used to estimate the values of P. As shown, the value of P with air is very close to the transitional value (recall that $P_x \sim 0.27$ for H_3PO_4 cathodes), and therefore the double-Tafel-slope region is relatively narrow.

5.2.2 Polymer-Electrolyte Fuel-Cell (PEFC) Cathodes

Workers at LANL have compiled an impressive amount of data on pressurized PEFC's. Of particular interest are the half-cell data presented in a paper by Springer *et al.* [63], which compared experimental results with a model the authors developed. Fig. 5-4 is a Tafel plot of the data points that were presented on a linear plot in Fig. 15 of this previous paper [75]. In their discussion of this figure the authors noted that, "The ratio of currents measured on 5 atm neat oxygen and on 5 atm air around a cathode potential of 0.8 V are around 2, rather than around 5. The model parameter required to account for this behavior is the limited ionic conductivity of the catalyst layer." This behavior, as well as the explanation offered, agree with Region 3 of the present polymer-electrolyte model.

As shown in Fig. 5-4, both the oxygen and air data exhibit approximately double Tafel slopes at ~ 0.8 V *vs.* RHE, and the oxygen dependence is shown for three different potentials in Fig. 5-5 for these two sets of data. In this case, the transitions to a double Tafel slope do not occur at the same current density; this discrepancy is probably due to gas-phase mass-transport effects becoming significant around this transitional current

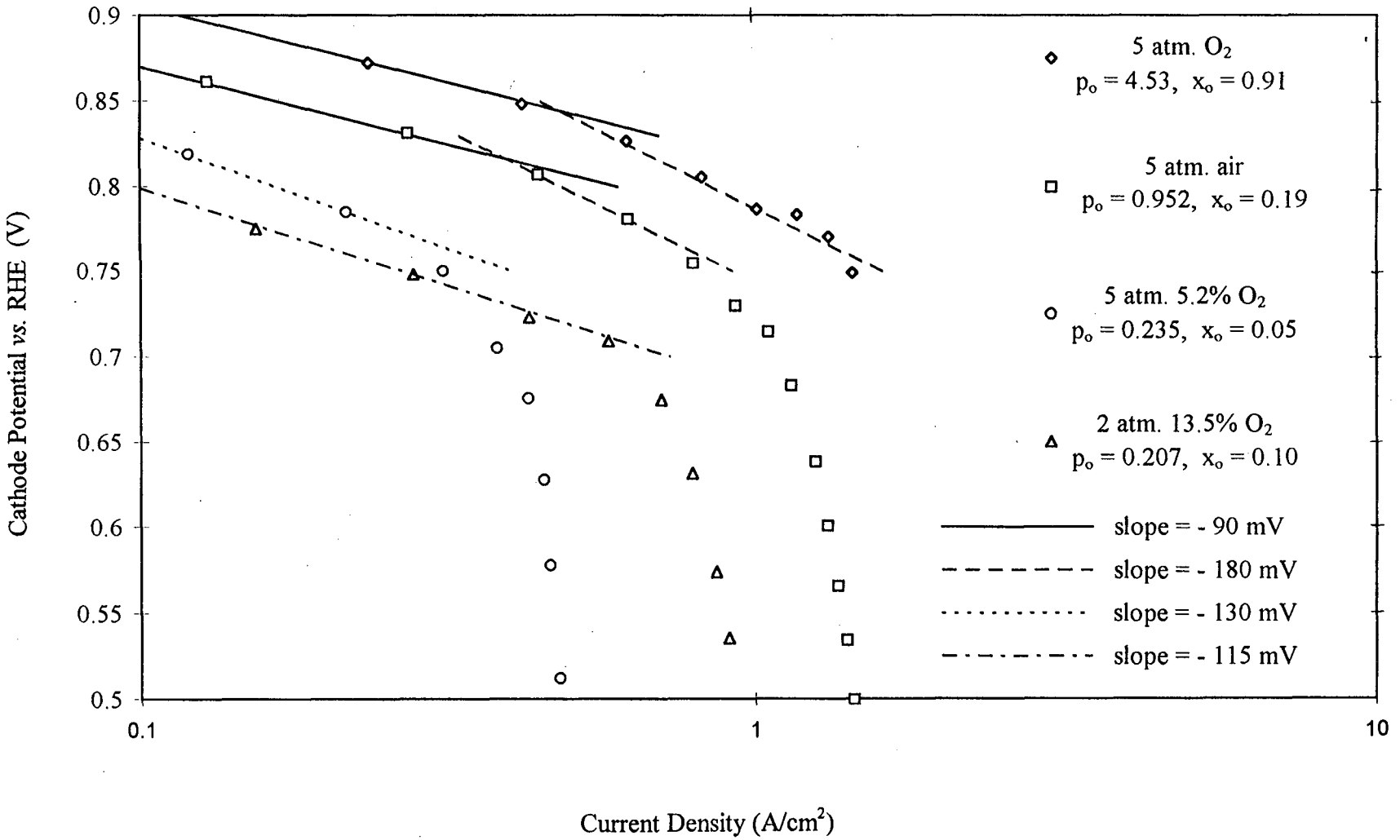

Figure 5-4. Tafel plot of PEFC cathode performance taken at 80° C, as reported by Springer *et al.* [63, 75].

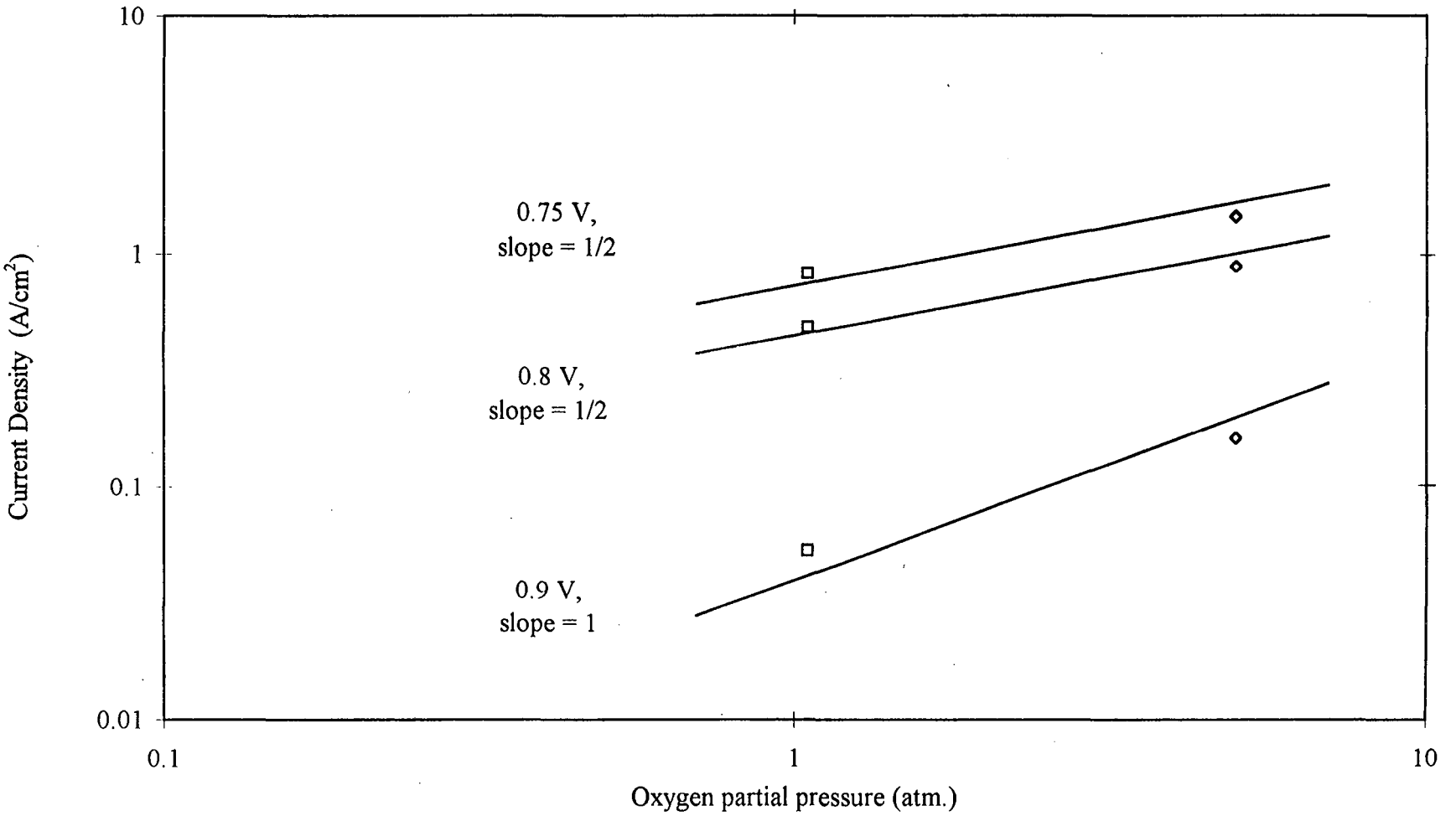

Figure 5-5. Oxygen dependence of data shown in Fig. 5-4 at three different cathode potentials.

density with the relatively low concentration of oxygen present in the air feed. (The mole fraction of oxygen for each of these feeds is given in Fig. 5-4, with the assumption that the gas streams are completely humidified.)

The other two sets of data shown in Fig. 5-4 were recorded with very low partial pressures of oxygen, and therefore one might expect that these cathodes would be controlled by oxygen transport at relatively low current densities. In fact, it is apparent from the high initial Tafel slopes shown here that mass transport plays a significant role, in addition to kinetics, at current densities as low as 100 mA/cm^2. Furthermore, if one calculates the ratio of the limiting currents, adjusted for the small difference in the oxygen partial pressures (*i.e.*, [0.235 atm / 0.207 atm] × [1.03 A/cm^2 / 0.489 A/cm^2] = 2.4), it is approximately equal to the ratio of the total pressures for these two sets of data. Therefore, one may conclude that these limiting currents are due to gas-phase mass-transport limitations.

In order to change the volume of the active layer which is conducive to oxygen transport relative to the volume which provides for ionic transport in a state-of-the-art PEFC, which contains no PTFE, one may vary the equivalent weight of the PFSA polymer used in the active layer. A lower equivalent weight generally equates to less fluorocarbon chains per ionic sulfonate group. This explains why cathodes impregnated with the dissolved Dow membrane (equivalent weight ≈ 900) display lower performance than similar electrodes impregnated with Nafion® (equivalent weight ≈ 1100), despite the superior performance of the Dow membrane as a PEFC electrolyte [37]. The higher concentration of hydrophobic-fluorocarbon regions in the Nafion® provides a higher concentration of oxygen in these electrodes and, as long as the cathode demonstrates

Region 1 or 2 behavior, the higher equivalent weight PFSA will be the preferred material for the active layer. However, if the cathode is controlled by ionic transport then this will not necessarily be the case.

5.3 Conclusions

The results of the models presented in the previous chapter provide a useful means for determining what mass-transport processes may be controlling a given fuel-cell cathode. By recording data under selective conditions, one may minimize the effects that are not taken into account by these models and thereby produce results which may be readily analyzed in the manner discussed above. It is generally useful to record such data up to the limiting currents, since these values may often provide interesting insights into the specific factors which control the cathode behavior at these high rates. Additionally, for a cathode with an agglomerate-type structure, one may discover the existence of a quadruple Tafel slope in this region; and this discovery may be used to obtain an estimate of the parameter P, which is a qualitative ratio of the importance of ionic and dissolved oxygen transport. All of this information may then be used to optimize the structure and operating conditions of the cathode for a particular application.

Abbreviations

AFC = alkaline fuel cell

ACFC = aqueous-carbonate fuel cell

DMFC = direct-methanol fuel cell

GDE = gas-diffusion electrode

GE = General Electric Company

IEMFC = ion-exchange-membrane fuel cell

LANL = Los Alamos National Laboratory

MEA = membrane-electrode assembly

ORR = oxygen reduction reaction

PAFC = phosphoric-acid fuel cell

PEFC = polymer-electrolyte fuel cell

PFSA = perflourosulfonic acid

PTFE = polytetrafluorethylene

RHE = reference hydrogen electrode

Notation

a_a = area of active catalyst per unit volume of an agglomerate, cm^{-1}

b = normal Tafel slope = $-\partial V/\partial \log i$, V

c_i = concentration of species i, mol/cm^3

D_i = diffusion coefficient of species i, cm^2/s

$\mathscr{D}_i$ = effective diffusivity of species i in a porous medium, cm^2/s

F = Faraday's constant, 96487 C/equiv

i_n = local current density, A/cm^2

i_o = exchange current density, A/cm^2

i_2 = current density in electrolyte phase, A/cm^2

i^* = dimensionless current density, defined by Fig. 4-3 and Table 4-2

i^* = dimensionless current density, defined by Fig. 4-6

I_a = current in an agglomerate, A

k = reaction rate constant, cm/s

k' = pH-independent rate constant, cm/s

L = thickness of active layer, cm

n = number of electrons transferred in electrode reaction

N_i = flux of species i, mol/cm^2·s

p_o = partial pressure of oxygen, atm

P = dimensionless parameter, defined by Eqn. 4-18

r = radial coordinate, cm

R = universal gas constant, 8.3143 J/mol·K

R_a = radius of an agglomerate particle, cm

R_{ORR} = reaction rate of the oxygen reduction reaction, mol/cm^3·s

t_i = transference number of species i

T = absolute temperature, K

u_i = mobility of species i, cm^2·mol/J·s

V = electrode potential, V

x = active layer coordinate, cm

z_i = charge number of species i

β = dimensionless parameter used in Eqns. 5-1 and 5-2

γ_i = reaction order with respect to species i

ε_a = agglomerate porosity

ε_l = porosity of active layer

η = overpotential, V

θ = parameter defined by Eqn. 4-14 (= $\gamma_{\pm}/2 - 2.3RT/2bz_{\pm}F$)

κ = conductivity of solution, S/cm

κ_e = effective conductivity of solution in porous media, S/cm

ν_i = number of ions into which a molecule of electrolyte dissociates

ρ_a = density of agglomerates in the active layer, cm^{-3}

τ_a = agglomerate tortuosity factor

ϕ = dimensionless parameter, defined by Eqn. 4-23

ϕR_a = Thiele modulus

Φ_i = electric potential of phase i, V

ψ = dimensionless potential parameter, defined by Eqn. 4-15

ψ_p = dimensionless potential parameter, defined by Eqn. 4-22

Superscripts

b = bulk

o = surface concentration in polymer-electrolyte model

s = surface concentration in liquid-electrolyte model

* = dimensionless value

+ = cations

- = anions

Subscripts

a = agglomerate

e = electrolyte

l = active layer

o = oxygen

p = polymer electrolyte

x = transitional value

+ = cations

- = anions

1 = solid phase

2 = electrolyte phase

1-2 = single-to-double Tafel-slope transition

2-4 = double-to-quadruple Tafel-slope transition

References

1. H. A. Liebhafsky and E. J. Cairns, *Fuel Cells and Fuel Batteries*, John Wiley & Sons, Inc., New York (1968).

2. L. J. M. J. Blomen and M. N. Mugerwa, eds., *Fuel Cell Systems*, Plenum Press, New York and London (1993).

3. K. Kinoshita, F. R. McLarnon, and E. J. Cairns, *Fuel Cells. A Handbook*, Prepared for the U. S. Dept. of Energy, Office of Fossil Energy, DOE/METC-88/6096 (1988).

4. O. Lindstrom, "That Incredible Fuel Cell, Part 1," *Chemtech*, **18**, 490 (1988), "Fuel Cell Power Plants, Part 2," *Chemtech*, **18**, 553 (1988), "Muscles, Engines, and Fuel Cells, Part 3," **18**, *Chemtech*, 686 (1989), and "Fuel Cell Markets, Part 4," *Chemtech*, **19**, 44 (1989).

5. A. J. Appelby, "Fuel Cell Technology and Innovation," *J. Power Sources*, **37**, 223 (1992).

6. R. A. Lemons, "Fuel Cells for Transportation," *ibid.*, **29**, 251 (1990).

7. P. G. Patil, "U. S. Department of Energy Fuel Cell Program for Transportation Applications," *ibid.*, **37**, 172 (1992).

8. S. Srinivasan, "Electrode Kinetics and Electrocatalytic Aspects of Electrochemical Energy Conversion", in *Electrochemistry In Transition* (O. J. Murphy, S. Srinivasan, and B. E. Conway, eds.), p. 577, Plenum Press, New York, NY (1992).

9. B. R. Rauhe, F. R. McLarnon, and E. J. Cairns, "Direct Anodic Oxidation of Methanol on Supported Platinum/Ruthenium Catalyst in Aqueous Cesium Carbonate," *J. Electrochem. Soc.*, **142**, 1073 (1995).

10. K. A. Striebel, "Oxygen Reduction in Fuel Cell Electrolytes," Ph.D. Thesis, University of California, Berkeley (1987).

11. K. A. Striebel, F. R. McLarnon, and E. J. Cairns, "Steady-State Model for an Oxygen Fuel Cell Electrode with an Aqueous Carbonate Electrolyte," *Ind. Eng. Chem. Res.*, **34**, 3632 (1995).

12. K. Kinoshita, *Electrochemical Oxygen Technology,* p. 171, John Wiley & Sons, Inc., New York, NY (1992).

13. R. S. Yeo, "Intrinsic Conductivity of Perfluorosulfonic Acid Membranes and its Implication to the Solid Polymer Electrolyte (SPE) Technology," in *Proceedings of the Symposium on Transport Processes in Electrochemical Systems*, (R. S. Yeo, T. Katan, and D. T. Chin, eds.), p.178, The Electrochemical Society, Inc., Pennington, NJ, (1982).

14. W. G. F. Grot, "Perflourinated Ion Exchange Polymers and Their Use in Research and Industry," *Macromol. Symp.* **82**, 161 (1994).

15. I. D. Raistrick, "Electrode Assembly for Use in a Solid Polymer Electrolyte Fuel Cell," *U. S. Patent 4,876,115*, (1989).

16. I. D. Raistrick, "Modified Gas Diffusion Electrode for Proton Exchange Membrane Fuel Cells," in *Proceedings of the Symposium on Diaphragms, Separators, and Ion-Exchange Membranes* (J. W. Van Zee, R. E. White, K. Kinoshita, and H. S. Burney, eds.), p. 172, The Electrochemical Society, Inc., Pennington, NJ, (1986).

17. A. Parthasarathy, C. R. Martin, and S. Srinivasan, "Investigations of the O_2 Reduction Reaction at the Platinum/Nafion® Interface Using a Solid-State Electrochemical Cell," *J. Electrochem. Soc.*, **138**, 916 (1991).

18. X. Ren, T. A. Zawodzinski, F. Uribe, H. Dai, and S. Gottesfeld, "Methanol Cross-over in Direct Methanol Fuel Cells," in *Proton Conducting Membrane Fuel Cells I*, (S. Gottesfeld, G. Halpert, and A. Landgrebe, eds.), p.284, The Electrochemical Society, Inc., Pennington, NJ, (1995).

19. S. R. Narayanan, H. Frank, B. Jeffries-Nakamura, M. Smart, W. Chun, G. Halpert, J. Kosek, and C. Cropley, "Studies on Methanol Crossover in Liquid-Feed Direct Methanol PEM Fuel Cells," *ibid.*, p. 278.

20. E. J. Cairns, "The Anodic Oxidation of Hydrocarbons and the Hydrocarbon Fuel Cell," in *Advances in Electrochemistry and Electrochemical Engineering, Vol. 8*, (C. W. Tobias, ed.), p. 337, John Wiley & Sons, Inc., New York, NY (1971).

21. p. 491 of Ref. [1].

22. J. Newman and W. Tiedemann, "Porous-Electrode Theory with Battery Applications," *AIChE Journal,* **21**, 25 (1975).

23. R. P. Iczkowski and M. B. Cutlip, "Voltage Losses in Fuel Cell Cathodes," *J. Electrochem. Soc.,* **127**, 1433 (1980).

24. P. N. Ross, Jr., "Anomalous Current Ratios in Phosphoric Acid Fuel Cell Cathodes," *LBL Report 13955*, (1986).

25. J. Giner and C. Hunter, "The Mechanism of Operation of the Teflon-Bonded Gas Diffusion Electrode: A Mathematical Model," *J. Electrochem. Soc.*, **116**, 1124 (1969).

26. L. G. Austin, "Tafel Slopes for Flooded Diffusion Electrodes," *Trans. Faraday Soc.*, **60**, 1319 (1964).

27. E. A. Ticianelli, C. R. Derouin, A. Redondo, and S. Srinivasan, "Methods to Advance Technology of Proton Exchange Membrane Fuel Cells," *J. Electrochem. Soc.*, **135**, 2209 (1988).

28. M. S. Wilson, personal communication, July 1995.

29. M. S. Wilson and S. Gottesfeld, "Thin-film Catalyst Layers for Polymer Electrolyte Fuel Cell Electrodes," *J. App. Electrochem.*, **22**, 1 (1992).

30. M. S. Wilson and S. Gottesfeld, "High Performance Catalyzed Membranes of Ultra-low Pt Loadings for Polymer Electrolyte Fuel Cells," *J. Electrochem. Soc.*, **139**, L28 (1992).

31. M. S. Wilson, J. A. Valerio, and S. Gottesfeld, "Low Platinum Loading Electrodes for Polymer Electrolyte Fuel Cells Fabricated Using Thermoplastic Ionomers," *Electrochim. Acta,* **40**, 355 (1995).

32. M. Uchida, Y. Aoyama, N. Eda, and A. Ohta, "New Preparation Method for Polymer-Electrolyte Fuel Cells," *J. Electrochem. Soc.,* **142**, 463 (1995).

33. L. W. Niedrach, "The Performance of Hydrocarbons in Ion Exchange Membrane Fuel Cells," *ibid.*, **109**, 1092 (1962).

34. E-TEK, Inc. 1995 Catalogue, *Gas Diffusion Electrodes and Catalyst Materials*, Natick, MA. (1995).

35. H. Binder, A. Kohling, H. Krupp, K. Richter, and G. Sandstede, "Electrochemical Oxidation of Certain Hydrocarbons and Carbon Monoxide in Dilute Sulfuric Acid," *J. Electrochem. Soc.,* **112**, 355 (1965).

36. E. J. Cairns and E. J. McInerney, "High Activity Platinum Electrocatalyst for the Direct Anodic Oxidation of Saturated Hydrocarbons," *J. Electrochem. Soc.,* **114**, 980 (1967).

37. O. J. Murphy, G. D. Hitchens, and D. J. Manko, "High Power Density Proton-Exchange Membrane Fuel Cells," *J. Power. Sources*, **47**, 353 (1994).

38. J. M. Prausnitz, R. N. Lichtenthaler, and E. G. de Azevedo, *Molecular Thermodynamics of Fluid-Phase Equilibria*, Second Edition, pp. 404-412, Prentice-Hall Inc., Englewood Cliffs, NJ (1986).

39. P. G. T. Fogg and W. Gerrard, *Solubility of Gases in Liquids*, pp. 35-37, John Wiley & Sons, New York, NY (1991).

40. See, for example, P. G. T. Fogg and W. Gerrard, *ibid.*, pp. 113-172, and references therein.

41. M. Falk, "An Infrared Study of Water in Perfluorosulfonate (Nafion) Membranes," *Can. J. Chem.*, **58**, 1495 (1980).

42. S. W. Capeci, P. N. Pintauro, and D. N. Bennion, "The Molecular -Level Interpretation of Salt Uptake and Anion Transport in Nafion Membranes," *J. Electrochem. Soc.*, **136**, 2876 (1989).

43. K. Kinoshita, *Electrochemical Oxygen Technology,* pp. 8-11, John Wiley & Sons, Inc., New York, NY (1992).

44. A. J. Appleby, "Electrocatalysis," in *Modern Aspects of Electrochemistry, No. 9*, (B. E. Coneway and J. O'M. Bockris, eds.) p. 369, Plenum Press, New York, NY (1974).

45. H. A. Gasteiger, N. Markovic, P. N. Ross, Jr., and E. J. Cairns, "Temperature Dependent Methanol Electro-Oxidation on Well-Characterized Pt-Ru Alloys," *J. Electrochem. Soc.*, **141**, 1795 (1994).

46. H. A. Gasteiger, N. Markovic, P. N. Ross, Jr., and E. J. Cairns, "CO Electro-oxidation on Well-Characterized Pt-Ru Alloys," *J. Phys. Chem.*, **98**, 617 (1994).

47. P. N. Ross, Jr., "Voltage Losses in Fuel Cell Cathodes", *J. Electrochem. Soc.*, **127**, 2655 (1980).

48. R. B. Bird, W. E. Stewart, and E. N. Lightfoot, *Transport Phenomena,* pp. 542-546, John Wiley and Sons, Inc., New York, NY (1960).

49. J. S. Newman, *Electrochemical Systems*, 2nd edition, p. 249, Prentice-Hall, Inc., Englewood Cliffs, NJ (1991).

50. K. Kinoshita, *Carbon: Electrochemical and Physiochemical Properties*, pp. 262-267, John Wiley and Sons, Inc., New York, NY (1988).

51. A. Pebler, "Transmission Electron Microscopic Examination of Phosphoric Acid Fuel Cell Components," *J. Electrochem. Soc.*, **133**, 9 (1986).

52. A. J. Appelby,"Fuel Cell Electrolytes: Evolution, Properties, and Future Prospects," *J. Power Sources*, **49**, 15 (1994).

53. L. S. Darken and H. F. Meier, "Conductances of Aqueous Solutions of the Hydroxides of Lithium, Sodium, and Potassium at 25° C," *J. Am. Chem. Soc.*, **64**, 621 (1942).

54. N. F. Shevchenko, V. V. Aleksanddrov, N. I. Gancharova, and T. N. Seredenko, "Determination of the Acidity of Concentrated Phosphoric Acid Solutions by Surface-Potential Stabilization," *Soviet Electrochem.*, **15**, 306 (1979).

55. B. R. Scharifker, P. Zelany, and J. O'M. Bockris,"The Kinetics of Oxygen Reduction in Molten Phosphoric Acid at High Temperatures," *J. Electrochem. Soc.*, **134**, 2714 (1987).

56. R. E. Davis, G. L. Horvath, and C. W. Tobias, "The Solubility and Diffusion Coefficient of Oxygen in Potassium Hydroxide Solutions," *Electrochim. Acta*, **12**, 287 (1967).

57. D. B. Sepa, M. V. Vojnovic,and A. Damjanovic,"Reaction Intermediates as a Controlling Factor in the Kinetics and Mechanism of Oxygen Reduction at Platinum Electrodes," *ibid*, **26**, 781 (1981).

58. J. S. Newman, *Electrochemical Systems*, 2nd edition, pp. 539-555, Prentice-Hall, Inc., Englewood Cliffs, NJ (1991).

59. T. E. Springer, T. A. Zawodzinski, and S. Gottesfeld, "Polymer Electrolyte Fuel Cell Model," *J. Electrochem. Soc.*, **138**, 2334 (1991).

60. T. F. Fuller and J. Newman,"Water and Thermal Management in Solid-Polymer-Electrolyte Fuel Cells," *ibid.*, **140**, 1218 (1993).

61. D. M. Bernardi and M. W. Verbrugge, "A Mathematical Model of the Solid-Polymer-Electrolyte Fuel Cell," *ibid.*, **139**, 2477 (1992).

62. Z. Ogumi, Z. Takehara, and S. Yoshizawa, "Gas Permeation in SPE Method," *ibid.*, **131**, 769 (1984).

63. T. E. Springer, M. S. Wilson and S. Gottesfeld, "Modeling and Experimental Diagnostics in Polymer Electrolyte Fuel Cells," *ibid.*, **140**, 3513 (1993).

64. T. E. Springer, T. A. Zawodzinski, M. S. Wilson, and S. Gottesfeld, "Characterization of Polymer Electrolyte Fuel Cells Using AC Impedance Spectroscopy," *ibid.*, **143**, 587 (1996).

65. T. A. Zawodzinski, C. Derouin, S. Radzinski, R. J. Sherman, V. T. Smith, T. E. Springer, and S. Gottesfeld, "Water Uptake and Transport Through Nafion® 117 Membranes," *ibid.*, **140**, 1041 (1993).

66. P. Schroeder, "Über Erstarrungs und Quellungserscheinungen von Gelatine", *Z. Phys. Chem.*, **45**, 75 (1903).

67. A. Parthasarathy, S. Srinivasan, A. J. Appelby, and C. R. Martin, "Temperature Dependence of the Electrode Kinetics of Oxygen Reduction at the Platinum/Nafion® Interface – A Microelectrode Investigation," *J. Electrochem. Soc.*, **139**, 2530 (1992).

68. H. S. Fogler, *Elements of Chemical Reaction Engineering*, 2nd edition, pp. 610-620, Prentice-Hall, Inc., Englewood Cliffs, NJ (1992).

69. J. S. Newman and C. W. Tobias, "Theoretical Analysis of Current Distribution in Porous Electrodes", *J. Electrochem. Soc.*, **109**, 1183 (1962).

70. A. Winsel,"Beiträge zur Kenntnis der Stomverteilung in porösen Elektroden", *Zeitschrift für Elektrochemie,* **66**, 287 (1962).

71. A. J. Appelby, "Carbon Components in the Phosphoric Acid Fuel Cell – An Overview," in *Proceedings of the Workshop on The Electrochemistry of Carbon* (S. Sarangapani, J. R. Akridge, and B. Schumm, eds.), p. 251, The Electrochemical Society, Inc., Pennington, NJ, (1983).

72. J. Newman, "Optimization of Potential and Hydrogen Utilization in an Acid Fuel Cell," *Electrochim. Acta*, **24**, 223 (1979).

73. H. R. Kunz and G. A. Gruver, "The Catalytic Activity of Platinum Supported on Carbon for Electrochemical Oxygen Reduction in Phosphoric Acid," *J. Electrochem. Soc.*, **122**, 1279 (1975).

74. T. Maoka, "Electrochemical Reduction of Oxygen on Small Platinum Particles Supported on Carbon in Concentrated Phosphoric Acid – I. Effects of Platinum Content in the Catalyst Layer and Operating Temperature of the Cathode," *Electrochim. Acta*, **33**, 371 (1988).

75. Special thanks to Dr. M. S. Wilson for providing this data in tabular form.

Appendix A: Computer Programs for Fuel-Cell Cathode Models

The following programs are written in FORTRAN, and they both call on the sub-routine BAND, which is provided by Newman [58], to provide a numerical solution.

```
C     Liquid-Electrolyte Model Program
      IMPLICIT REAL*8 (A-H,O-Z)
      COMMON A(4,4),B(4,4),C(4,2001),D(4,9),G(4),X(4,4)
     %,Y(4,4),NX,NJ,T,psi
      DIMENSION CONC(2001)
C     SET # OF MESH POINTS, NJ, AND # OF EQNS, NX.
      NJ=1001
      NX=1
C     CALC MISC CONSTANTS. T = dimensionless parameter theta
C                          P = dimensionless parameter P
C                          PSI = dimensionless electrolyte potential
      T=0.75d0
      p=1000.0d0
      psi=1.0d0
      H=1.0d0/dble(NJ-1)
C
C     BEGIN ITERATIVE PROGRAM. Start w/ electrolyte conc. in electrode
C                              equal to bulk electrolyte.
C                              CONC = dimensionless electrolyte conc.
      JCOUNT=0
      DO 2 J=1,NJ
2     CONC(J)=1.0d0
 5    JCOUNT=JCOUNT+1
      J=0
C     CALC DIMENSIONLESS PARAMETER:
C                                    POT=dimensionless Thiele modulus
      X(1,1)=0
      Y(1,1)=0
 10   J=J+1
      POT=(CONC(J)**T)*DEXP(PSI/2)
      A(1,1)=0
      B(1,1)=0
      D(1,1)=0
      IF(J.NE.1) GO TO 12
C     BOUNDARY CONDITION AT ELECTRODE/ELECTROLYTE INTERFACE. AT J=1, CONC=1
      G(1)=-CONC(J)+1.0
      B(1,1)=1.0
      CALL BAND(J)
      GO TO 10
 12   IF(J.EQ.NJ) GO TO 15
C     STATE EQUATIONS FOR INTERIOR OF ELECTRODE.  1 < J < NJ
      COTHJ=1.0d0/TANH(POT)
      G(1)=-1.0/H/H*(CONC(J-1)-2.0*CONC(J)+CONC(J+1))+P*(POT*COTHJ-1.0)
      A(1,1)=1.0/H/H
      D(1,1)=1.0/H/H
      B(1,1)=-2.0/H/H-P*T*POT/CONC(J)*(COTHJ+POT*(1.0-COTHJ*COTHJ))
      CALL BAND(J)
      GO TO 10
```

```
C     BOUNDARY CONDITON AT ELECTRODE/GAS INTERFACE. J=NJ
 15   G(1)=-1.0/2.0/H*(CONC(J-2)-4.0*CONC(J-1)+3.0*CONC(J))
C     %(log(CONC(J-2))-4.0*log(CONC(J-1))+3.0*log(CONC(J)))
      B(1,1)=3.0/2.0/H
      A(1,1)=-2.0/H
      Y(1,1)=1.0/2.0/H
      CALL BAND(J)
      DO 16 J=1,NJ
c     shoe horn
      if (C(1,J).LT.-0.99*CONC(J)) C(1,J)=-0.99*CONC(J)
 16   CONC(J)=CONC(J)+C(1,J)
      LCV = 1

       DO 19 J=1,NJ
 19    IF ((ABS(C(1,J)).GT.1.e-6*ABS(CONC(J)))) LCV = 0
       IF ((LCV.EQ.0).AND.(JCOUNT.LT.40)) GO TO 5
       DCYO=(-3.d0*CONC(1)+4.d0*CONC(2)-CONC(3))/2.d0/H
       DO 21 J=1,NJ,100
 21    PRINT *,J,CONC(J)
       print *, 'jcount, p ,psi ',jcount,p,psi
       PRINT *,'conc (@ y=1)',CONC(nJ)
       PRINT *,'dc/dy (@ y=0)',-DCYO
 C     CALCULATE AVERAGE ELECTROLYTE CONCENTRATION
       TOTAL=0.0d0
       DO 30 J=0,NJ
 30    TOTAL=CONC(J)+TOTAL
       AVE=TOTAL*H
       print *,"ave. electrolyte conc. =",ave
 c     Define minimum conc. (at electrode/gas interface) for OXY subroutine
       CONM=CONC(NJ)
       CALL OXY(PSI)
       IF (LCV.EQ.0) PRINT *,'THIS RUN DID NOT CONVERGE'
       END

       SUBROUTINE OXY(PSI)
 C     CALCULATES OXYGEN PROFILES AND AVERAGE OXYGEN CONCENTRATION
       IMPLICIT REAL*8 (A-H,O-Z)
       DIMENSION COX(1000)
       print *,'psi =', psi
       print *,'OXYGEN PROFILES IN AGGLOMERATE PARTICLES @ y=0 (c=1):'
       NRT=10000
       H=1.0d0/dble(NRT)
       COX(0)=dexp(PSI/2)/dsinh(dexp(PSI/2))
       DO 50  NR=1,NRT
       R=dble(NR)/NRT
 50    COX(NR)=(dsinh(dexp(PSI/2)*R)/dsinh(dexp(PSI/2)))/R
       DO 60 NR=0,NRT,1000
       R=dble(NR)/NRT
 60    print *,'R=',R,'  Co=',COX(NR)
 C     calculate average oxygen concentration
       TOTAL=0.0d0
       DO 80 NR=0,NRT
 80    TOTAL=COX(NR)+TOTAL
       AVE=TOTAL*H
       print *,"ave. O2 conc. =",ave
       end
```

```
C     PROGRAM FOR POLYMER ELECTROLYTE CATHODE - 2 PHASE MODEL
      IMPLICIT REAL*8 (A-H,O-Z)
      COMMON A(4,4),B(4,4),C(4,2001),D(4,9),G(4),X(4,4)
     %,Y(4,4),NX,NJ
      DIMENSION COX(2001), P(2001)
C     SET # OF MESH POINTS, NJ, AND # OF EQNS, NX.
      NJ=1001
      NX=2
C     INPUT MISC CONSTANTS AND VARIABLE.
C                              POT=dim. overpotential (at x=0)
C                              phi=nF(DoCo)/b*kappa

      POT=5.0d0
      phi=1.d-2
      H=1.0d0/dble(NJ-1)
C
C     BEGIN ITERATIVE PROGRAM. Start w/ dim. oxygen conc. equal to bulk
C                              COX(J)=1
      JCOUNT=0
      DO 2 J=1,NJ
      p(j)=pot
 2    COX(J)=1.0d0
 5    JCOUNT=JCOUNT+1
      J=0
      do 6 i=1,nx
      do 6 k=1,nx
      X(i,k)=0.d0
    6 Y(i,k)=0.d0
 10   J=J+1
      do 8 i=1,nx
      g(i)=0.d0
      do 8 k=1,nx
      A(i,k)=0.d0
      B(i,k)=0.d0
    8 D(i,k)=0.d0
      IF(J.NE.1) GO TO 12
C     BOUNDARY CONDITIONS AT ELECTRODE/ELECTROLYTE INTERFACE, @ J=1, (X=0)
C       (1) dCo/dX = 0  and, (2) set P = POT
      G(1)=-1.d0/2.d0/H*(-3.d0*COX(J)+4.d0*COX(J+1)-COX(J+2))
      B(1,1)=-3.d0/2.d0/H
      D(1,1)=2.0d0/H
      X(1,1)=-1.d0/2.d0/H
      G(2)=POT-P(J)
      B(2,2)=1.d0
      CALL BAND(J)
      GO TO 10
 12   IF(J.EQ.NJ) GO TO 15
C     STATE EQNS FOR 1<J<NJ,  (1) d2Co/dX = COX*exp(P)
C                             (2) d2P/dX  = phi*COX*exp(P)
      G(1)=-1.d0/H/H*(COX(J-1)-2.d0*COX(J)+COX(J+1))+COX(J)*DEXP(P(J))
      A(1,1)=1.d0/H/H
      D(1,1)=1.d0/H/H
      B(1,1)=-2.d0/H/H-DEXP(P(J))
      B(1,2)=-COX(J)*DEXP(P(J))
      G(2)=-1.d0/H/H*(P(J-1)-2.d0*P(J)+P(J+1))+phi*COX(J)*DEXP(P(J))
      A(2,2)=1.d0/H/H
      D(2,2)=1.d0/H/H
      B(2,2)=-2.d0/H/H-phi*COX(J)*DEXP(P(J))
      B(2,1)=-phi*DEXP(P(J))
      CALL BAND(J)
```

```
      GO TO 10
C     BOUNDARY CONDITONS AT ELECTRODE/GAS INTERFACE, @ J=NJ,   (X=1)
C          (1)  Co = 1  and   (2)  dP/dX = 0
 15   G(1)=1.d0-COX(J)
      B(1,1)=1.d0
      G(2)=-(P(J-2)-4.d0*P(J-1)+3.d0*P(J))
      A(2,2)=-4.d0
      B(2,2)=3.d0
      Y(2,2)=1.d0
      CALL BAND(J)
c      print *, ' jcount ',jcount,cox(1),p(nj)
      DO 16 J=1,NJ
C     "Shoe Horn" for Co
      if (C(1,J).LT.-0.99d0*COX(J)) C(1,J)=-0.99d0*COX(J)
 16   COX(J)=COX(J)+C(1,J)
      DO 17 J=1,NJ
C     "Shoe Horn" for P
c      if (C(2,J).LT.-0.99d0*P(J)) C(2,J)=-0.99d0*P(J)
       if (C(2,J).LT.-1.d0) C(2,J)=-1.d0
       if (C(2,J).gT. 1.d0) C(2,J)= 1.d0
 17   P(J)=P(J)+C(2,J)
      LCV1 = 1
      LCV2 = 1
      DO 18 J=1,NJ
 18   IF ((dABS(C(1,J)).GT.(1.d-6*dABS(COX(J))))) LCV1= 0
      DO 19 J=1,NJ
 19   IF ((dABS(C(2,J)).GT.(1.d-6*dABS(P(J))))) LCV2 = 0
      LCV = LCV1+LCV2
      IF ((LCV.EQ.0).AND.(JCOUNT.LT.40)) GO TO 5
C     CALC DESIRED OUTPUTS:
C                                DCX1 = dCo/dX  (@X=1)
C                                DPX0 = dP/dX   (@X=0)
      DCX1=(COX(NJ-2)-4.d0*COX(NJ-1)+3.d0*COX(NJ))/2.d0/H
      DPX0=(-3.d0*P(1)+4.d0*P(2)-P(3))/2.d0/H
C     PRINT DESIRED OUTPUTS:
      print *, 'jcount, phi, POT ',jcount,phi,POT
      PRINT *,'conc. of O2(@ x=1) =',COX(NJ)
      PRINT *,'conc. of O2(@ x=0) =',COX(1)
      PRINT *,'overpotential(@ x=0) =',P(1)
      PRINT *,'overpotential(@ x=1) =',P(NJ)
      print *,'dCo/dx(@ x=1)=', DCX1
      PRINT *,'i*=i/del=phi*[-dCo/dx(@ x=1)] =',-phi*DCX1
      PRINT *,'i*=i/del=[dP/dx(@ x=0)] =',DPX0
      DO 20 J=1,NJ,100
  20  PRINT *,'J,COX', J,COX(J)
      DO 22 J=1,NJ,100
  22  PRINT *,'J,dim OP', J,P(J)
      DO 24 J=1,NJ,100
  24  PRINT *,'J,local i', J,COX(J)*DEXP(P(J))
      IF (LCV.EQ.0) PRINT *,'THIS RUN DID NOT CONVERGE'
      END
```

Appendix B: Derivation of Asymptotic Solutions of Eqn. 4-16

Eqn. 4-16 may be expressed as:

$$\frac{\partial^2 c_e^*}{\partial x^{*2}} = P\left[\phi R_a \coth\left(\phi R_a\right) - 1\right] \qquad \text{(B-1)}$$

where $\phi R_a = [(c_e^*)^\theta \exp(\psi/2)]$.

Asymptotic solutions of this equation are obtained by first noting that for small values of ϕR_a, which corresponds to relatively high potentials (*i.e.*, Regions 1 and 3 with low current densities), $[\phi R_a \coth(\phi R_a) - 1] \rightarrow (\phi R_a)^2 / 3$, and for large values of ϕR_a, which corresponds to low potentials (*i.e.*, Regions 2 and 4), $[\phi R_a \coth(\phi R_a) - 1] \rightarrow (\phi R_a - 1) \approx \phi R_a$. Four analytic solutions result from these two asymptotes by assuming that the electrolyte concentration is fairly uniform at relatively low current densities (*i.e.*, setting $c_e^* \approx 1$ for all x^* for Regions 1 and 2) and is very nonuniform at high current densities (*i.e.*, setting $c_e^* << 1$ at $x^* = 1$ for Regions 3 and 4). The complete derivations of the four asymptotic solutions are given below.

Region 1

Using $[\phi R_a \coth(\phi R_a) - 1] \rightarrow (\phi R_a)^2 / 3$, Eqn. B-1 becomes:

$$\frac{\partial^2 c_e^*}{\partial x^{*2}} \approx \frac{P}{3}\left(c_e^*\right)^{2\theta} \exp(\psi) \qquad \text{(B-2)}$$

then, setting $c_e^* \approx 1$ for all x^* and applying the boundary condition at $x^* = 1$, yields:

$$\frac{\partial c_e^*}{\partial x^*} \approx \frac{P}{3}\exp(\psi)\left(x^* - 1\right) \qquad \text{(B-3)}$$

Therefore:

$$i^* \equiv -\left.\frac{\partial c_e^*}{\partial x^*}\right|_{x^*=0} \approx \frac{P}{3}\exp(\psi) \tag{B-4}$$

Region 3

Here again we start with Eqn. B-2. Let $q = dc_e^* / dx^*$, then:

$$\frac{\partial^2 c_e^*}{\partial x^{*2}} = \frac{1}{2}\frac{dq^2}{dc_e^*} \approx \frac{P}{3}\left(c_e^*\right)^{2\theta}\exp(\psi) \tag{B-5}$$

$$q = \left[\frac{2P}{3}\exp(\psi)\int\left(c_e^*\right)^{2\theta} dc_e^*\right]^{\frac{1}{2}} \tag{B-6}$$

Integrating and assuming that $c_e^* << 1$ at $x^* = 1$, yields:

$$i^* \equiv -\left.\frac{\partial c_e^*}{\partial x^*}\right|_{x^*=0} \approx \sqrt{\frac{2/3P}{2\theta+1}}\exp(\psi/2) \tag{B-7}$$

Region 2

Using $[\phi R_a \coth(\phi R_a) - 1] \rightarrow (\phi R_a - 1) \approx \phi R_a$, Eqn. B-1 becomes:

$$\frac{\partial^2 c_e^*}{\partial x^{*2}} \approx P\left(c_e^*\right)^{\theta}\exp(\psi/2) \tag{B-8}$$

then, setting $c_e^* \approx 1$ for all x^* and applying the boundary condition at $x^* = 1$, yields:

$$\frac{\partial c_e^*}{\partial x^*} \approx P\exp(\psi/2)\left(x^* - 1\right) \tag{B-9}$$

Therefore:

$$i^* \equiv -\left.\frac{\partial c_e^*}{\partial x^*}\right|_{x^*=0} \approx P\exp(\psi/2) \qquad \text{(B-10)}$$

Region 4

Here again we start with Eqn. B-8. Let $q = dc_e^* / dx^*$, then:

$$\frac{\partial^2 c_e^*}{\partial x^{*2}} = \frac{1}{2}\frac{dq^2}{dc_e^*} \approx P\left(c_e^*\right)^\theta \exp(\psi/2) \qquad \text{(B-11)}$$

$$q = \left[2P\exp(\psi/2)\int\left(c_e^*\right)^\theta dc_e^*\right]^{\frac{1}{2}} \qquad \text{(B-12)}$$

Integrating and assuming that $c_e^* << 1$ at $x^* = 1$, yields:

$$i^* \equiv -\left.\frac{\partial c_e^*}{\partial x^*}\right|_{x^*=0} \approx \sqrt{\frac{2P}{\theta+1}}\exp(\psi/4) \qquad \text{(B-13)}$$

Ernest Orlando Lawrence Berkeley National Laboratory
One Cyclotron Road | Berkeley, California 94720

Prepared for the U.S. Department of Energy under Contract No. DE-AC03-76SF00098